Quaternary Science Reviews 324 (2024) 108462

Contents lists available at ScienceDirect

Quaternary Science Reviews

journal homepage: www.elsevier.com/locate/quascirev

Late Quaternary morpho-stratigraphic record of diapir rise in the Cardona salt extrusion, NE Spain. Halokinetic sequences, raised terraces and uplift rates

Guillermo Pérez-Villar [a], Francisco Gutiérrez [a,*], Mario Zarroca [b], Carles Roqué [c], Alfonso Benito-Calvo [d], Anna Menció [c]

[a] Departamento de Ciencias de la Tierra, Universidad de Zaragoza, C/. Pedro Cerbuna 12, 50009, Zaragoza, Spain
[b] Geology Department, Universitat Autònoma de Barcelona, E-08193, Bellaterra, Barcelona, Spain
[c] Grup de Recerca en Geologia Aplicada i Ambiental, GAiA), Área de Geodinámica Externa, Departamento de Ciencias Ambientales, Facultad de Ciencias, Universitat de Girona, E-17003, Girona, Spain
[d] CENIEH, Paseo Sierra de Atapuerca 3, Burgos, 09002, Spain

ARTICLE INFO

Handling Editor: Dr Giovanni Zanchetta

Keywords:
Erosional unroofing
Passive diapir
Halokinetic deformation
Uplifted terrace
Salt-rise rate

ABSTRACT

Active diapirism has received very limited attention from the geomorphological and Quaternary Science perspective, despite the role played by this ground deformation process in the development of landforms and sedimentary environments, and the important practical implications associated with mobile salt structures (e,g., mining, hydrocarbon production, geostorage). The Cardona salt extrusion (NE Spain) was initiated in late Quaternary times from the post-shortening unroofing of the crest of a salt anticline by the entrenchment of the transverse Cardener River. Detailed mapping, outcrop analysis, geophysical data and trenching indicate that the diapir-flanking deposits show halokinetic complexes comprising two types of morpho-stratigraphic units: (1) an older flap of coarse-grained drapefolded colluvial deposits; and (2) younger lacustrine and fluvial deposits in peripheral depressions confined between the upturned colluvial flaps and the country rock slope. These synkinematic units record an overall relief inversion and correspond to the so-called wedge and hook halokinetic sequences, recording ratios between diapir rise rate and sedimentation rate lower and greater than 1, respectively. The radiocarbon ages obtained from several raised late Holocene strath terraces carved in the salt indicate uplift rates within the range of 36.5–12.1 mm/yr, consistent with geodetic data. The spatial variability of the uplift rates can be related to increasing flow rates towards the axis of the salt wall and potential along-strike variations. The relatively high diapir rise rates observed at Cardona diapir, unaffected by contractional displacement loading (tectonic squeezing), is attributed to the youthful stage of the salt extrusion and the low dynamic viscosity of the Cardona Saline Formation, with a low proportion of impurities and a significant amount of potash salts.

1. Introduction

Active diapirism and the associated long-term ground displacement has implications for Quaternary Science and Geomorphology: (1) creation of morpho-sedimentary environments (e.g., withdrawal basins; Pilcher et al., 2011; Gutiérrez et al., 2019); (2) landform development (e.g., morpho-structural domes, salt domes and glaciers; giant landslides; Talbot and Pohjola, 2009; Gutiérrez et al., 2012, 2023; Kravitz et al., 2017); (3) deformation of recent deposits and landforms (Bruthans et al., 2010); (4) drainage disruption (Martin and Bouma, 1981; Colman, 1983; Gutiérrez and Lizaga, 2016); (5) karst rejuvenation and development of multi-level cave systems (Frumkin, 1996). Additionally, instability in surface and subsurface environments related to salt flow is of major concern from the applied perspective, given the special interest of diapirs for mining of salt and other minerals, hydrocarbon production, and geostorage activities (e.g., Warren, 2016), including radioactive waste repositories (Köthe et al., 2007).

Three styles of diapir growth can be differentiated (Jackson and

* Corresponding author.
E-mail addresses: perezvillarguillermo@gmail.com (G. Pérez-Villar), fgutier@unizar.es (F. Gutiérrez), mario.zarroca.hernandez@uab.cat (M. Zarroca), scutellinia@gmail.com (C. Roqué), alfonso.benito@cenieh.es (A. Benito-Calvo), anna.mencio@udg.edu (A. Menció).

https://doi.org/10.1016/j.quascirev.2023.108462
Received 11 July 2023; Received in revised form 26 October 2023; Accepted 3 December 2023
Available online 14 December 2023

Hudec, 2017): (1) *reactive diapirism,* when salt flows upward to fill the space created by extension beneath a faulted and thinned overburden; (2) *active diapirism*, when buried salt rises arching, piercing and shouldering aside an overburden; and (3) *passive diapirism*, when salt emerges at the surface and rises without the restraining effect of a roof. Steep passive diapirs (salt stocks and salt walls) can grow vertically in the floor of subsiding basins with concomitant salt rise and peripheral aggradation (downbuilding) to form salt structures more than 10 km high. The stratigraphic and structural features of the sediments accumulated in the flank of passive diapirs largely depend on the ratio between net diapir rise and sedimentation rate, which determines the topographic expression of the emergent diapir (i.e., molding ratio). Wedge halokinetic sequences form when sedimentation rate exceeds diapir rise and the deposits onlap and encroach the diapir. Hook halokinetic sequences record periods of relatively slow sedimentation in which salt rise tends to restrict deposition to the periphery of the diapir. Wedge and hook halokinetic sequences are characterized by wide versus narrow zones of bed thinning, and deformation and convergent versus parallel sequence boundaries, respectively (Rowan et al., 2003; Giles and Rowan, 2012). Both sequences, with growth stratal geometries, are shouldered aside and folded by the rising salt to form upturned flaps with drape monoclinal structure (Jackson and Hudec, 2017; Rowan et al., 2020).

Active and passive diapirism can be driven by two mechanisms that may operate in combination: buoyancy related to density inversion, and more significantly, differential loading (Jackson and Hudec, 2017). Differential loading can be induced by displacement loading related to horizontal tectonic forces (e.g., squeezing of a diapir by shortening) and vertical gravitational loading. Salt flow driven by differential gravitational loading without the interplay of significant lateral tectonic forces (i.e., halokinesis) can be related to elevation changes in the top-salt topography and/or variations in the weight of the overburden. The spatial changes in the overburden load can be due to tectonic and earth surface processes, such as the stacking of thrust sheets, prograding sediment wedges (Ge et al., 1997), advancing and retreating ice-sheets (Sirocko et al., 2002; Lang et al., 2014), or the excavation of erosional depressions (Huntoon, 1982; Schultz-Ela and Walsh, 2002). Fluvial incision may have two important effects on diapirism. Firstly, the excavation of valleys creates differential loading conditions that may drive salt flow towards the erosionally unloaded valley. Secondly, fluvial entrenchment may locally breach the overburden (erosional unroofing) leading to the initiation of passive diapirism and salt extrusion. Gutiérrez et al. (2019) compiled case studies that illustrate active salt flow related to erosional unloading, providing information on the geomorphic and stratigraphic effects, as well as data on surface displacement rates.

Salt structures have been extensively investigated from the stratigraphic and structural perspective, largely because of their significance for hydrocarbon exploration (Warren, 2016; Jackson and Hudec, 2017). It is estimated that around 60% of hydrocarbon fields worldwide area associated with salt structures or bedded salt unaffected by salt tectonics (Halbouty, 1979). However, studies addressing the morpho-sedimentary effects of rising diapirs and the assessment of long-term displacement rates using deformed landforms and deposits in combination with geochronological data are very scarce. Table 1 compiles works including long-term uplift rates calculated for passive diapirs (salt stocks and salt walls in subaerial and submarine erosional environments) using numerically dated Quaternary morpho-stratigraphic markers. It is important to note that salt rise rate in diapirs may show significant spatial variations, typically decreasing towards the edge where resistance to flow imposed by the country rock increases (e.g., Pirazzoli et al., 2004; Bruthans et al., 2010).

This work is focused on the Cardona salt extrusion, a passive diapir initiated by the post-shortening erosional unroofing of the crest of a salt anticline in the southern folded foreland of the Pyrenees (Ebro Cenozoic Basin, NE Spain). The main goals of the investigation include: (1) analyzing the initiation and Quaternary evolution of the salt extrusion and the development of morpho-sedimentary environments created by the upwelling of salt; (2) characterizing and dating for the first time diapir-flanking Late Pleistocene to Holocene halokinetic sequences deposited in an erosional continental environment; and (3) estimating long-term uplift rates using radiocarbon-dated deposits. Active salt rise at Cardona was noticed since Roman times. The Roman writer Aulo Gelio (125-180 AD), in his book Noctes Atticae (book II, chapter XXII), indicated "fodinae pulcherrimae mons ex sale mero magnus: quantum demas, tantum acrescit", meaning "an enormous mountain of pure salt, the more you extract, the more it grows". This information is derived from the previous book "Origins" by Marco Porcio Catón (Catón de Old; 234-149 BC) that reports on mining activities in the Hispania Citerior (Andreu Galera, Cardona Archive, pers. comm.). This is most probably the first written account to active diapirism. Several authors referred to uplifted and upturned deposits of putative Plio-Quaternary age (Villafranquian) associated to the Cardona salt extrusion (Wagner et al., 1971; Riba et al., 1975; Masana and Sans, 1996; Sans and Koyi, 2001). Sans and Koyi, 2001 indicated that leveling measurements carried out

Table 1
Long-term uplift rates calculated for passive salt diapirs (lacking a restraining roof) in erosional environments using dated morpho-stratigraphic markers in different tectonic environments.

Diapir	Tectonic environment	Driving mechanism	Deformation marker	Uplift rate	Reference
Mount Sedom salt wall, Dead Sea, Israel	Releasing bend in active strike-slip fault	Local extension and overburden loading	Lisan Fm. lake deposits (+75 m; ~15.5 ka)	~5 mm/yr	Weinberger et al. (2006)
			Multi-level cave passages (+46-5 m; 8–0.7 ka)	≤6–7 mm/yr	Frumkin (1996)
Namakdam salt stock, Zagros Mountains, Iran	Shortening in collisional environment	Squeezing of precursor diapir (displacement loading)	Marine terraces, fluvial terraces and cave levels (≤135 m; ≤55 ka)	4 mm/yr	Bruthans et al. (2010)
			Raised beaches (+22-4 m; 5.7–1.1 ka)	2–10 mm/yr	Pirazzoli et al. (2004)
			Marine terraces (+12-11 m; 5.6–5.3 ka)	6 mm/yr	Reyss et al. (1999)
Jabal al Salif salt wall, Read Sea Rift, Yemen	Extensional	Extension and overburden loading	Coral reefs (+17 m; 3.7 ka)	4.6 mm/yr	Davison et al., 1996
Wedehof Diapir	Extensional	Extension and overburden loading	Post-glacial uplift (+50 m; ca. 130 ka)	0.4 mm/yr	Sirocko et al. (2002)
Navarrés salt wall, Iberian Chain, Spain	Extensional	Probable extension and erosional unloading related to fluvial erosion	Calcareous tufa terraces (+30-13 m; 241-79 ka)	0.1–0.4 mm/yr	Gutiérrez et al. (2019)
Alaminos Canyon diapir, Gulf of Mexico continental slope, USA	Passive margin	Erosional unloading in a submarine canyon 550–750 m deep	Biostratigraphically dated domed deposits (400 m; 18-11 ka)	20–40 mm/yr	Martin and Bouma (1981)
Weeks Island salt dome, USA	Passive margin	Differential overburden loading	Loess deposit (+50 m; 25 ka)	2 mm/yr	Autin (2002)
Colorado Plateau, USA	Stable continental region	Erosional unloading by fluvial entrenchment	Upwarped strath terrace	0.5–0.6 mm/yr	Jochems and Pederson (2015)

between 1979 and 1986 (at an unknown place) yielded mean uplift rates of 1 mm/yr. Preliminary DInSAR data indicate uplift rates of the order of 10–20 mm/yr in the NE sector of the salt extrusion, where vertical displacement is not affected by mining subsidence (Rodríguez-Lloveras et al., 2020).

2. Geological and geomorphological setting

The Cardona salt extrusion is located in the northeastern sector of the Ebro Cenozoic Basin (NE Spain), which is the southern foreland basin of the Pyrenees, an Alpine orogen resulting from the collision between the Iberian and European plates (Late Cretaceous-Miocene). Here, the Ebro Basin is bounded by the Pyrenees to the north and the Catalan Coastal Ranges to the southeast, and the sedimentary fill essentially consists of folded Paleogene formations. The basin fill displays an overall regressive evolution with marine sedimentation followed by deposition in continental environments within an endorheic basin (Riba et al., 1983; Sáez and Riba, 1986; Pardo et al., 2004) (Fig. 1).

The lower marine succession records an Eocene transgression-regression cycle represented by the Igualada Marls Formation (Bartonian-early Priabonian) and the overlying Cardona Saline Formation (Priabonian; late Eocene) (Fig. 1). The late Eocene Cardona Saline Formation was deposited during the Priabonian regression along the southern foredeep of the Pyrenees (Riba et al., 1983; Rosell and Pueyo, 1997). The wedge-shaped Cardona Saline Formation, extensively investigated via boreholes, mine galleries and seismic reflection profiles, had an initial thickness of around 300–350 m (Pueyo, 1975). This marine formation, with substantial amounts of K–Mg chlorides, comprises the flowing units from base to top (Pueyo, 1975; Rosell and Pueyo, 1997): (1) the 5 m thick Basal Anhydrite Member; (2) the 130–200 m thick Lower Halite Member; (3) the 70–100 m thick Potash Member, including the sylvite-bearing subunit (5–20 m), the carnallite-bearing subunit (40–80 m); and the top salt subunit (10–20 m); and (4) the 35 m thick Grey Marls with anhydrite and halite (or Top Grey Lutites).

In the late Eocene, uplift along the basin margins related to the development of compressional structures transformed the Ebro Basin into a land-locked endorheic basin, dictating the onset of terrestrial sedimentation (Riba et al., 1983; Puigdefàbregas et al., 1986). The depositional scheme during this late Eocene-early Oligocene continental phase was characterized by lacustrine environments with evaporitic and carbonate sedimentation in the deeper parts of the basin, grading laterally towards the margins into alluvial environments (Fig. 1). The lacustrine sediments are represented by the Barbastro Gypsum Formation, the Torá Siltstone Formation, and the Castelltallat Limestone Formation (Anadón et al., 1989). These lithostratigraphic units interdigitate laterally with clastic successions derived from the Pyrenees (Suria Formation, Solsona Formation, Berga Conglomerate Formation) and the Catalan Coastal Ranges (Artés Molasse Formation and the Montserrat and Sant Llorenç de Munt Conglomerate Formation) (Sáez and Riba, 1986).

In Cardona area, the Cardona Saline Formation is overlain by the late Eocene-early Oligocene Suria Formation, around 400 m thick. This formation comprises a Lower Member ca. 100 m thick of thinly bedded grey mudstones and sandstones, and an Upper Member consisting of alternating red sandstones and mudstones (Riba et al., 1975). The Suria Formation is overlain by the Solsona Formation, made up of alternating yellowish red sandstones and mudstones. These two units have a vague gradational contact given by a change from sheet-like sandstone beds to more channel-shaped beds.

The Eocene-Oligocene formations in this sector of the Ebro foreland basin display a series of buckle folds detached along the Cardona Saline Formation, characterized by narrow salt-cored anticlines and broad intervening synclines (Fig. 1). These detachment folds show variable trends attributed to the orientation of the feather edge of the Cardona salt, where folding vanishes (Sans and Verges, 1995): (1) NW-SE in the northern sector; (2) NE-SW in the central and southern sector; and (3) WNW-ESE in the southwestern zone. The Cardona salt extrusion is associated with the NE-SW-trending Cardona-Pinós Anticline, roughly located in the area where the Cardona Saline Formation reached the greatest primary thickness (Sans, 2003). This anticlinal structure with an amplitude of around 1 km comprises two anticlines with a left-stepping relay pattern that overlap in the Cardona Diapir area; the 10 km long Cardona Anticline to the NE and the 30 km long Pinós Anticline to the SW (Riba et al., 1975; Sans, 2003) (Fig. 1). The Cardona Anticline has its southern termination around the SW edge of the Cardona salt extrusion. In the overlapping section, the Cardona and Pinós anticlines are separated by the 2 km long Intermediate Syncline, located on the SE margin of the Cardona Diapir (Riba et al., 1975). The Cardona Anticline in the section associated with the Cardona salt extrusion exhibits a SE-verging asymmetry, with dips of 30–50° and around 70–90° or even overturned in the NW and SE limbs, respectively. According to Sans and Koyi, 2001, in the Solsona Syncline northwest of the Cardona-Pinós Anticline the overburden reaches 2000 m thick and is welded with the infra-salt units, whereas in the Saló Syncline to the southeast the overburden reaches 1200 m in the axial zone and has not been welded. The initiation of the development of the Cardona-Pinós Anticline occurred sometime in the late Eocene-early Oligocene, during deposition of the Solsona Formation, based on the lack of thickness and facies changes across the anticline in the Suria and Barbastro formations, and the presence of growth stratal geometries (i.e., progressive unconformity) in the Solsona Formation on the southern limb of the anticline (Riba et al., 1975; Del Santo et al., 2000; Sans and Koyi, 2001). During the development of this detachment fold, the salt flowed from the synclines towards the low-pressure core of the anticline, favored by differential loading related to greater syntectonic aggradation and overburden thickness in the synclines (Sans and Verges, 1995; Sans and Koyi, 2001; Sans, 2003). The growth of the Cardona-Pinós Anticline probably ceased in early Miocene times, based on the available knowledge about the tectonic evolution of the Pyrenees and the Ebro foreland basin (Riba et al., 1975).

The NE-SW-trending anticlines in this sector of the Ebro foreland basin are dissected perpendicularly by the SE-flowing Cardener River, tributary of the Llobregat River (Fig. 1). The Cardona salt extrusion occurs in the floor and southwest margin of the Cardener River valley and has been attributed to the post-shortening piercement of the overburden in the crest of the Cardona Anticline, thinned by erosion (i.e., erosion-induced piercement; Sans and Koyi, 2001; Jackson and Hudec, 2017). The NE-SW oriented salt extrusion is 2 km long, 0.7 km wide and covers around 0.9 km^2. The geometry of the Cardona Diapir, which is a local protrusion rising from the crest of the salt core of the anticline, has been constrained using data from mining boreholes and galleries. It has a stem 250 m high and 250–500 m wide, and a bulb 80 m high and 400–700 m wide (Sans and Koyi, 2001). According to seismic profiles, the planar base of the salt, gently dip to the north, lies 1400 m below the Cardener River (1000 m b.s.l.; Riba et al., 1975). In the NE sector of the salt extrusion, close to the Cardener River, the salt-overburden contact shows an apparent conformable geometry. In contrast, in the SW sector the salt tends to juxtapose the overburden showing a discordant contact (i.e., diapiric), with upturned and sheared strata of the Suria Formation. This difference may be related to greater erosion at the diapir edge close to the Cardener River, rather than to a different behavior of the extruding salt. On the NE margin of the Cardener Valley, the hinge zone of the Cardener Anticline shows a significant plunge to the NE of 30°, with the consequent rapid deepening of the top of the salt away for the valley.

Sedimentation in the northeastern sector of the Ebro foreland basin ceased in late Oligocene or early Miocene times, when the depocenter of the basin migrated to the southern-central sector (Riba et al., 1983). During this period the area was probably dominated by erosion, despite it was located within an endorheic basin, but at a relatively high position above the base level. Rapid erosion and fluvial dissection of the basin fill started once it was captured by the external drainage network and

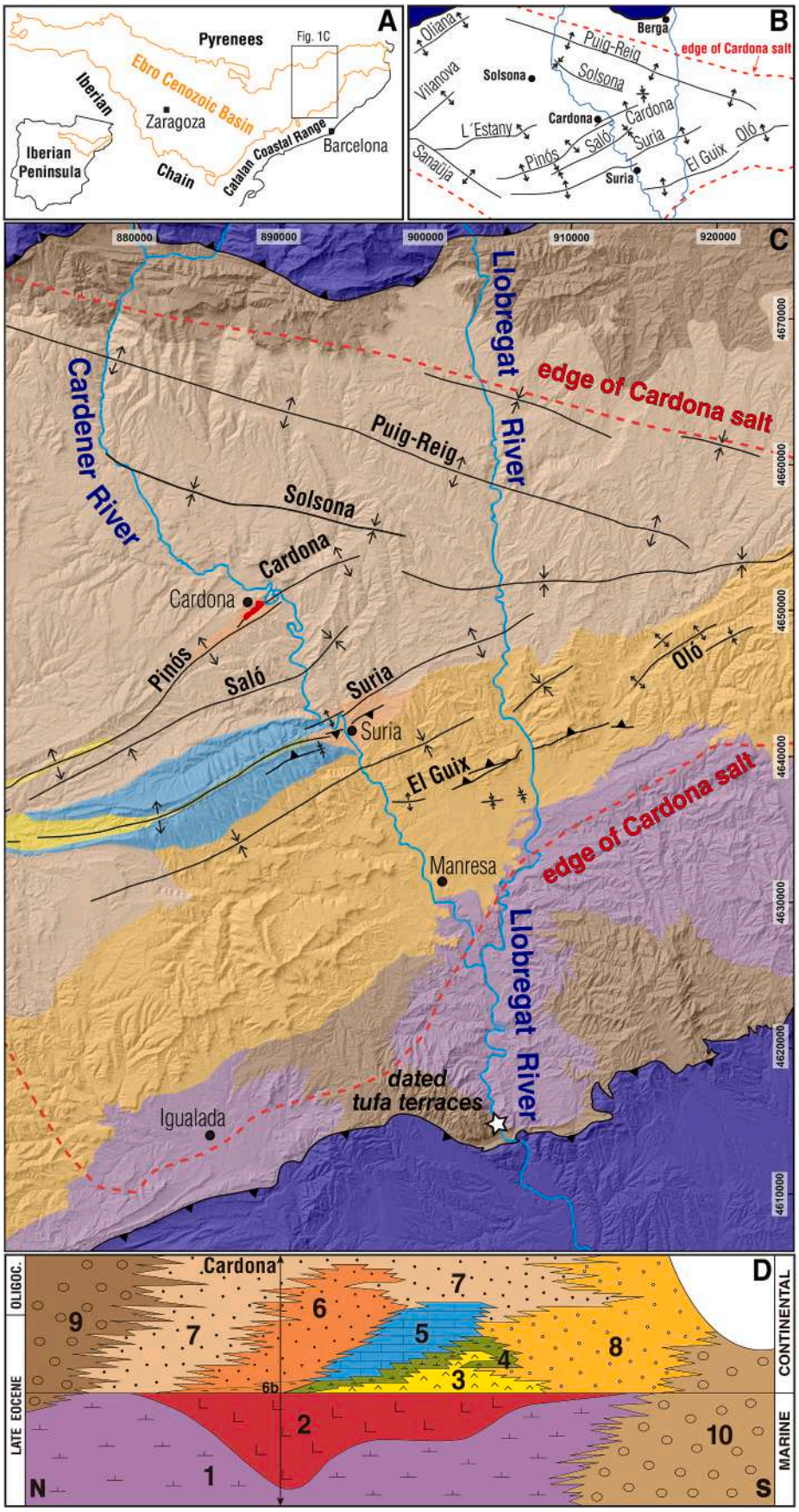

(caption on next page)

Fig. 1. Geological setting of the Cardona salt extrusion. A: Location of the study area within the Ebro Cenozoic Basin in NE Spain. B: Structural sketch of the foreland basin showing the distribution of folds detached along the Cardona Saline Formation, which feather edge controls fold trends (modified from Sans and Verges, 1995; Lucha et al., 2008). C: Shaded relief model showing the distribution of the lithostratigraphic units, folds, and the Cardona salt extrusion. Asterisk indicate location of calcareous tufa terraces of the Llobregat River dated by Luque and Julià (2007). D: Stratigraphic sketch showing the geometrical relationships of the main formations in the northeastern sector of the Ebro Basin in a N–S oriented transect. In Cardona area, the conformable contact between the Cardona Saline Formation (unit 2) and the Lower Member (subunit 6b) of the Suria Formation marks the change from marine to continental sedimentation (modified from Sáez and Riba, 1986). 1: Igualada Marls Fm.; 2: Cardona Saline Fm.; 3: Barbastro Gypsum Fm.; 4: Torá Silstone Fm.; 5: Castelltallat Limestone Fm.; 6: Suria Formation./: Solsona Fm.; 8: Artés Fm.; 9: Berga Conglomerate Fm.; 10: Montserrat and Sant Llorenç de Munt Conglomerate Fm.

opened to the Mediterranean Sea. The capture of the basin by the Ebro River has been roughly situated in the middle-late Miocene by magnetochronological data (Pérez-Rivarés et al., 2018) and landscape modelling (García-Castellanos et al., 2003). Unfortunately, no chronological data is available for the capture of the NE sector of the Ebro Basin by the Llobregat River, although a similar age can be assumed for the change from endorheic to exorheic conditions.

3. Methodology

Geophysical data were acquired across the southwestern edge of the salt extrusion by electrical resistivity imaging (ERI) and seismic refraction (SR) in order to investigate the subsurface geometry of deformed Quaternary deposits overlying and flanking the rising Cardona salt (Fig. 2). To our best knowledge, this is the first work documenting such type of geophysical investigation in a salt extrusion. ERI was considered a suitable method for capturing the resistivity contrast associated with the contact between the salt bedrock and the flap of upturned

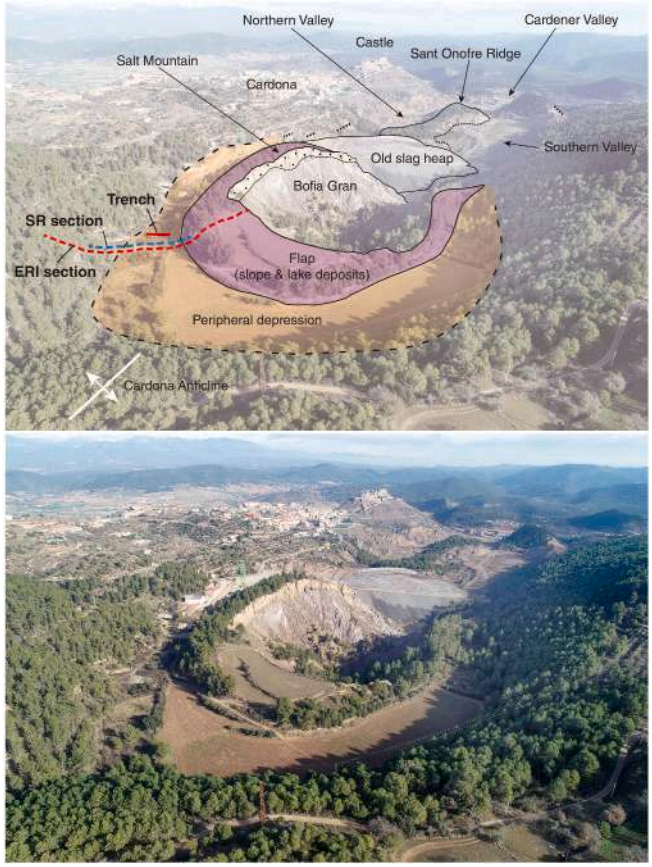

Fig. 2. Oblique view of the Cardona salt extrusion on the SW margin of the Cardener River. In the foreground, the dome-shaped Salt Mountain, covered by upwarped colluvial and lacustrine deposits (upturned flap) and carved by a large internally drained karst depression with extensive salt exposures (Bofia Gran). The location of the geophysical sections (ERI, SR) and trench across the peripheral depression of the Salt Mountain are indicated.

Quaternary deposits. The ERI data (ERI section) were collected with an ABEM Terrameter LS2 resistivimeter (Guideline Geo), 64 electrodes, and 4 cable sections. A smaller electrode spacing of 2.5 m was set for the two inner cable sections to increase resolution, while electrode spacing was 5 m in the outer ones. The measuring array was set to both gradient (GR) and dipole-dipole (DDP). The sensitivity function of DDP makes it very sensitive to lateral resistivity changes, but it can suffer from poor signal-to-noise ratios for the deepest resistivity levels. GR, in turn, offers moderate sensitivity to lateral resistivity variations, while its sensitivity to vertical variations and its signal noise ratio are somewhat more favorable than that of DDP (e.g., Dahlin and Zhou, 2004). Apparent resistivity records were inverted using the EarthImager2D (Advanced Geosciences, Inc.), based on the least-square smoothness-damping constrained method (Occam's inversion) (Constable et al., 1987; LaBrecque et al., 1996; Loke, 2011). The starting model was set to the average apparent resistivity of the gathered dataset, and the inversion method to the smooth model L2-norm (Loke et al., 2003). Topographic correction was performed by dump distortion using elevation data derived from a LiDAR-based bare-surface DEM with a horizontal resolution of 2 m from the Cartographic and Geological Institute of Catalonia, Spain.

The seismic refraction method was essentially applied to gain information on the geometry and depth of the cover-bedrock boundary based on the expected P-wave velocity increase, behaving as an effective refractor. A seismic refraction line (SR section) was acquired coinciding with the central portion of the ERI section using a Geode 24-channel seismograph (Geometrics) and 24 14Hz-vertical geophones spaced at 4 m (Fig. 2). A 5 kg sledgehammer was used as the power source. The different seismic traces were constructed by stacking 6 to 10 hammer impacts for each shot location. A total of 27 shots were performed at both ends of the lines and between adjacent geophones (SRT1). The dromochrones (travel time curves of the P-waves) were constructed by identifying the first arrivals with PickWin software (SeisImager2D-Geometrics). The velocity inversion was carried out with PlotRefa software (SeisImager2D-Geometrics) by means of an optimized tomographic analysis, based on an iterative least squares method (Geometrics, 2009). Topographic correction was carried out with the same DEM used for the ERI sections.

A backhoe trench was excavated in the bottom of the peripheral depression west of the Salt Mountain. The trench walls were cleaned and the SE side was gridded with horizontal and vertical strings at a spacing of 1 m. The selected wall was logged on graph paper at a scale of 1:50 after marking the stratigraphic contacts with color pins. A total of 18 samples of various types of organic material (charcoal, shell, organic sediment) were collected from deformed deposits exposed at the trench and in the investigated outcrops (Fig. 3; Table 2), in order to constrain the timing and rate of diapiric deformation by AMS radiocarbon dating. The conventional radiocarbon ages were corrected for total fractionation effects using the parameters outlined by Stuiver and Polach (1977). These ages were calibrated using the high probability density range method (BetaCal4.20) and the database INTCAL20 (Reimer et al., 2020). Additional details on the AMS radiocarbon method can be found in Moreno et al. (2021). The location of samples and the relative height above the corresponding base level have been measured with a DGPS. The elevation of the channel in valley sections buried by anthropogenic deposits has been established using a 1:2000 scale topographic map from 1962 with contour interval of 2 m.

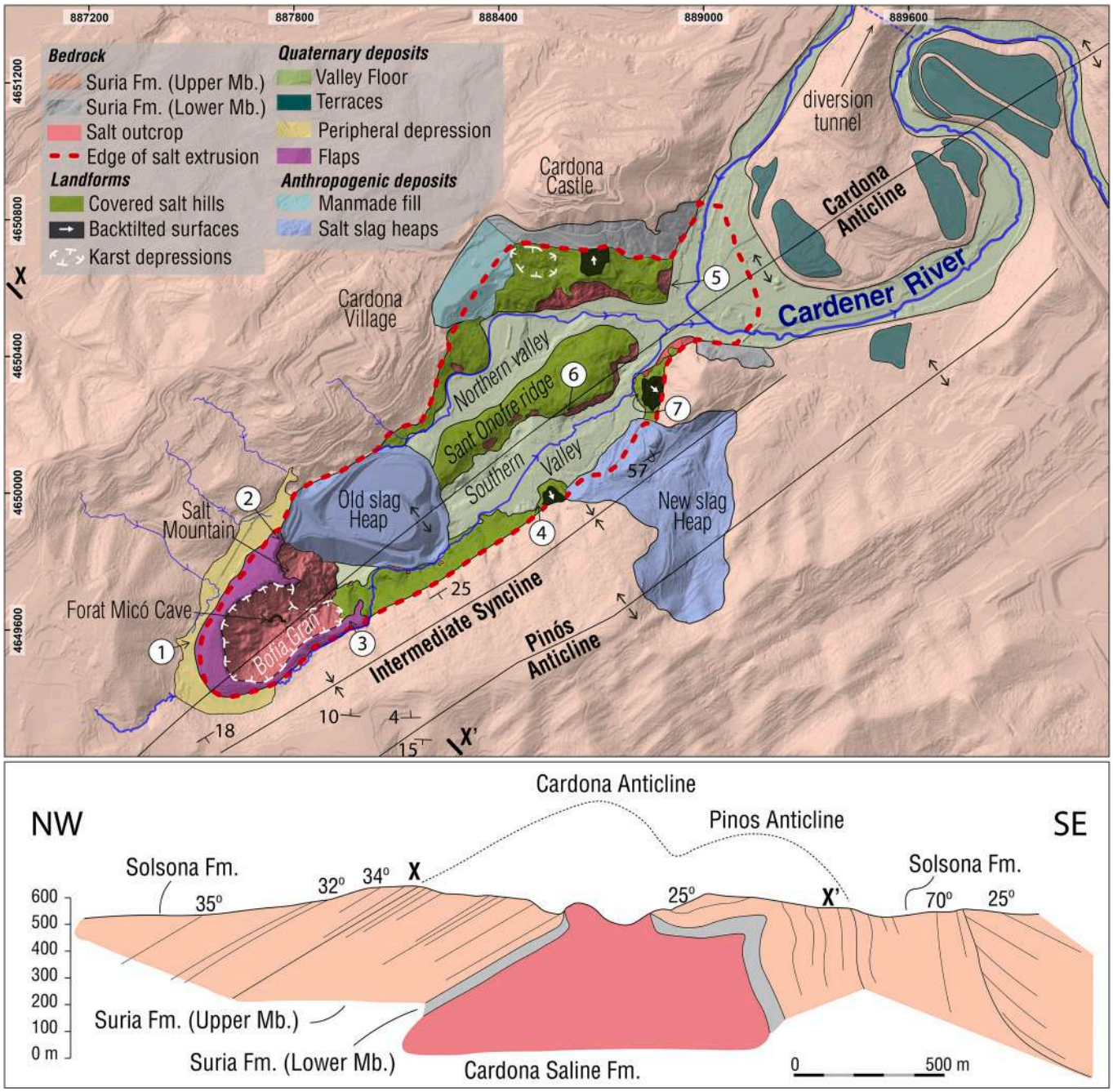

Fig. 3. Geological-gemorphological map showing the distribution of the main features and deformed Quaternary deposits and landforms associated with the Cardona salt extrusion. The trace of the central sector of the cross-section, modified from Riba et al. (1975), is indicated in the map. Note that the salt diapir is located within an erosional depression carved along the axial zone of the Cardona Anticline and surrounded by steep slopes underlain by sandstone and mudstone of the Suria Formation. The Cardener River used to traverse the NE sector of the diapir before its cut-off in 2000. The investigation sites have been labelled with numbers. Labels in map indicate investigation and sampling points.

4. Results

4.1. Distribution of deformed quaternary deposits and landforms

A detailed geological-gemorphological map of the salt extrusion has been produced based on thorough field surveys, paying special attention to Quaternary deposits and landforms that may be used as markers of halokinetic deformation (Fig. 3). Overall, the Cardona salt extrusion occurs in a NE-SW oriented erosional depression on the southwestern margin of the Cardener River valley, carved along the axial zone of the Cardona Anticline, where the salt core is closer to the surface. The depression is surrounded by steep slopes typically more than 100 m high underlain by sandstones and mudstones of the Suria Formation, dipping into the slope (i.e., limbs of the Cardona Anticline) (Figs. 2 and 3).

In the southwestern sector, the salt extrusion is expressed as a protruding hill (the Salt Mountain) with an overall domal geometry and a maximum local relief of 90 m (i.e., free board; Talbot, 1998) (Figs. 2 and 3). On the crest and steep flanks of this hill the salt is largely covered by flaps of deformed Quaternary deposits that protect the bedrock from dissolution. This prominent salt hill is carved by a polygenetic karst depression (the Bofia Gran) around 300 m long and 70 m deep that drains through a swallow hole at the upper entrance of the Forat Micó

Table 2
Radiocarbon dating results from the different investigation sites. Sample code, laboratory number provided by Beta Analytic, material, conventional ages and calibrated ages using the high probability density range method (BetaCal4.20) and the database INTCAL20 (Reimer et al., 2020). Figures in parentheses indicate the relative area under the probability curve.

Code	Laboratory number	Material	Conventional age (2σ) (yr BP)	Calibrated age (2σ) (yr BP)
Trench				
C-1	β-650655	Charred material	6080±30	(0.881) 7010 - 6848
				(0.052) 7153 - 7130
				(0.021) 6815 - 6800
C-2	β-650656	Charred material	5410±30	(0.896) 6291 - 6181
				(0.058) 6142 - 6120
C-10	β-650658	Charred material	1760±30	(0.954) 1716 - 1570
C-15	β-650659	Charred material	340±30	(0.954) 476 - 312
Northern lacustrine synkinematic sequence				
HALOK-1	β-663803	Shell	15620±50	(0.954) 18992 - 18802
HALOK-4	β-663805	Shell	14660±50	(0.954) 18175 - 17811
Southern lacustrine synkinematic sequence				
BAD 1.2	β-656715	Organic sediment	9310±40	(0.887) 10595 - 10371
				(0.046) 10653 - 10620
				(0.012) 10319 - 10304
				(0.009) 10353 - 10341
BAD4	β-650662	Charred material	11490±40	(0.945) 13463 - 13298
				(0.009) 13263 - 13254
CAR-530	β-647272	Charred material	12290±30	(0.888) 14333 - 14089
				(0.066) 14787 - 14725
Southern late Holocene valley fill				
Wedge-0	β-664247	Charred material	4550±30	(0.572) 5192 - 5051
				(0.351) 5320 - 5255
				(0.021) 5249 - 5232
				(0.01) 5225 - 5215
Wedge-1	β-663801	Charred material	1270±30	(0.837) 1287 - 1175
				(0.112) 1192 - 1122
				(0.004) 1088 - 1084
Strath terraces of the Cardener River				
CAR-CHAR1	β-647270	Wood	760 ± 30	(0.954) 728 - 664
CAR-CHAR2	β-647271	Wood	1210 ± 30	(0.859) 1180 - 1058
				(0.095) 1248 - 1210
CAR-CHAR3	β-650660	Charred material	1310±30	(0.954) 1294 - 1176
CAR-CHAR5	β-650661	Organic sediment	5360±30	(0.282) 6085 - 6003
				(0.245) 6217 - 6165
				(0.241) 6155 - 6108
				(0.186) 6277 - 6235
Strath terraces of the Southern Valley				
VAL-1b	β-663789	Charred material	870±30	(0.835) 800 - 688
				(0.111) 902 - 867
				(0.008) 820 - 812
VAL-4b	β −650662	Charred material	1240±30	(0.558) 1192 - 1070
				(0.396) 1271 - 1204
VAL-5	β-656723	Plant material	940±30	(0.954) 922 - 778

Cave (Fig. 3). The steep slopes on bare salt in this basin display remarkable karrenfields dominated by rillenkarren. The Salt Mountain is surrounded by a horseshoe-shaped depression situated between the marginal sandstone hillslopes and the inner domal Salt Mountain (Figs. 2 and 3). This peripheral depression 1.1 km long and 70 m wide has a flat and poorly drained floor, except in the southwest sector, where it has been incised by a gully. Both the upturned synkinematic deposits in the flaps associated with the Salt Mountain (labelled as 2 and 3 in Fig. 3) and the inset valley fill of the peripheral depression (labelled as 1 in Fig. 3) have been studied analyzing outcrops, geophysical data and a trench.

To the northeast of the Salt Mountain the depression carved along the salt core of the Cardona Anticline displays an axial salt ridge 750 m long and 35 m high (the Sant Onofre Ridge) flanked by two NE-flowing longitudinal valleys (Figs. 2 and 3). Here, for simplicity, the valleys are designated as the Northern Valley and the Southern Valley. The crest of the axial Sant Onofre ridge is underlain by colluvial and alluvial deposits, indicating that it was formerly located in a low lying area. This relief inversion can be related to: (1) deflection of the drainage towards the margins because of greater uplift in the axial zone of the diapir; and (2) the presence of less soluble evaporites in the inner sector of the diapir (i.e., halite versus potash salts). On the margins of the valleys associated with the edge of the diapir there are some anomalous salt hills with backtilted flat-top surfaces underlain by colluvial and alluvial deposits (Fig. 3). The steep valley-facing slopes of these hills locally display discontinuous salt outcrops and landslides. An exposed synkinematic sequence underlying a backtiled surface on the SE margin of the diapir has been analyzed (labelled as 4 in Fig. 3). Additionally, uplifted fluvial deposits lying on planar strath surfaces cut into the salt bedrock (i.e., strath terraces) have been dated on both margins of the Sothern Valley (labelled as 5, 6, 7 in Fig. 3).

The accumulation of two large halite slag heaps related to underground potash mining between the 1931 and 1990, plus numerous anthropogenic deposits have strongly modified the topography and hydrology of the salt extrusion (Cardona and Viver, 2002; Lucha et al., 2008) (Figs. 2 and 3). The “Old slag heap” was accumulated between the Salt Mountain and the Sant Onofre Ridge in the period 1925–1972, with 3 million tones and covering 12,6 ha. The “New slag heap” was dumped in the interval 1972–1990 on the Southern Valley and on the southeast margin of the diapir, amounting 7 million tones and covering 25.7 ha. This slag heap has been removed to take profit from the previously discarded halite.

In the northeast sector, the salt extrusion is dissected and traversed by the Cardener River, which displays a tight meander with SW-facing

convexity. The valleys floor has a broad gravelly channel and narrow floodplains dominated by fine-grained facies. The NE plunge of the Cardener Anticline determines the occurrence of outcrops of the Suria Fm. on the NE margin of the Cardener Valley. This resistant bedrock inhibits the excavation of an erosional depression on the NE valley margin equivalent to that of the opposite valley side. The Cardener River used to run at the foot of salt slopes on the SW margin of the valley, eventually excavating strath surfaces and depositing fluvial sequences on top of them. Here, we have identified and dated different uplifted strath terraces (labelled as 5 in Fig. 3). At Cardona, the Cardener River has a contributing area of 627 km^2 and has an average discharge of 2.4 m^3/s. The maximum peak discharge of the instrumental record of 257 m^3/s was measured in the flood of November 8, 1982. This section of the Cardener River associated with the salt extrusion was cut off in 2000 by a tunnel to mitigate a number of environmental and engineering problems (e.g., hydrochemical degradation of the river water, mine flooding, sinkhole development; Lucha et al., 2008).

4.2. Geophysical and trenching investigation in flap and peripheral depression

The 200 m long ERI sections were placed across the edge of the diapir on the western sector the Salt Mountain (Fig. 2 and point 1 in Fig. 3). Fig. 4 shows the image derived from the data collected with the Gradient array, which is similar to that of the Dipole-Dipole section. The ERI profile covered from west to east the following geomorphic domains (Fig. 2): (1) A steep slope underlain by inward dipping sandstone and mudstone beds of the Suria Formation. Here the bedrock is covered by a shallow landslide with a well-defined toe at the foot of the slope. (2) A low gradient and flat-bottomed valley developed along the peripheral depression of the Salt Mountain. In the investigation site the alluvium is overlain by a gravelly anthropogenic fill at least 2 m thick. (3) The flank and top of the domal relief created by the rising salt extrusion. Here, the salt is covered by upwarped colluvial deposits with angular sandstone boulders derived from the slope situated on the opposite margin of the valley. The planar top of the hill at the investigated section is related to artificial excavation for cultivation.

The eastern portion of the ERI section shows a very low resistivity unit (<10 Ωm) with a steep lateral edge attributable to decompressed damp salt. The salt is draped by a medium-high resistivity unit (>150 Ωm) ascribable to bouldery colluvium affected by a monoclinal drape fold. This unit continues and thickens beneath the valley fill, where it reaches around 15 m. The valley fill displays a lower clayey low resistivity unit (<30 Ωm; exposed in the trench) mantled by the less conductive man-made gravelly fill. The contact between the salt and the W-dipping Suria sandstone can be roughly situated beneath the foot of the steep slope underlain by the upturned colluvial flap and the lower hinge of the monocline. The geometrical relationships interpreted in the section indicates a valley fill: (1) inset with respect to the upturned portion of the colluvial unit; and (2) overlying it at the margin of the diapir. The seismic tomography refraction profile, restricted to the valley area, displays a similar configuration, including: (1) a low p-wave velocity (<1 km/s) valley fill with a probable channel-shaped base and a synform on the eastern side; (2) vaguely defined medium velocity (1–2 km/s) coarse colluvium beneath and next to the valley fill; and (3) high velocity (>2 km/s) undifferentiated bedrock.

The deposits of the peripheral depression of the Salt Mountain were investigated by a 20 m long and 3.3 m deep backhoe trench sited 30 m to

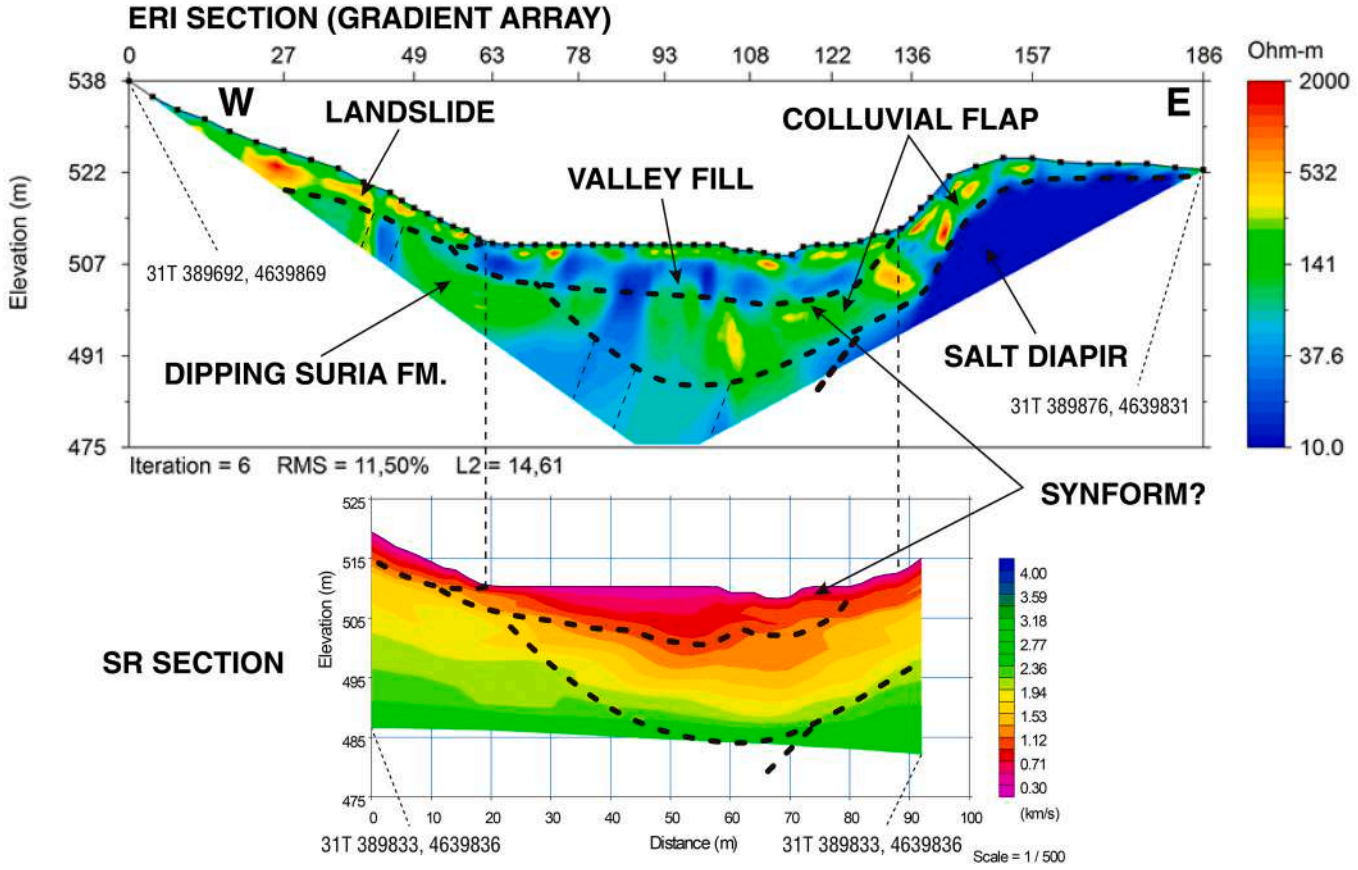

Fig. 4. Geophysical data collected across the western margin of the Cardona salt extrusion. The electrical resistivity image (ERI, Gradient array) covers the salt mountain draped by an upwarped colluvial flap, the adjacent and nested alluvium-filled peripheral depression, and a steep slope on Surian Fm. with a shallow landslide. The seismic tomography refraction section is restricted to the valley in the peripheral depression. See location of sections in Fig. 2. Horizontal scales in meters.

the NE of the seismic profiles, to avoid from the thick man-made fill (Fig. 2). Unfortunately, no permission was obtained for digging a trench in other a priori more adequate locations, like the crop fields situated to the SE and just at the foot of the slope of the rising hill. The trench was oriented perpendicularly to the depression (Fig. 5). Unfortunately, the excavation could not be extended to the base of the slope underlain by the upturned colluvial flap, where greater deformation can be expected. The trench essentially exposed alluvium dominated by fine-grained facies (units 1, 2, 4, 5, 6, 8) that interdigitate at the SE valley margin with coarse-grained colluvial facies (units 3, 7), mainly consisting of angular sandstone clasts. Four radiocarbon ages were obtained from the alluvial units in correct stratigraphic order: (1) unit 1, 7153-6800 cal yr BP; (2) unit 2, 6291-6120 cal yr BP; (3) unit 5, 1716-1570 cal yr BP; and (4) unit 8, 476-312 cal yr BP (age ranges at 2 sigma; BP = 1950 AD by convention). The alluvium was deposited by sporadic flow events in the ephemeral peripheral valley, whereas the colluvium was reworked from the adjacent over-steppened slope underlain by the upturned colluvial flap. The clayey alluvial facies correspond to the low resistivity and low P-wave velocity valley fill imaged in the ERI and SR sections (Fig. 2).

In the NW sector of the trench, units 3, 5, 6 and 7 have experienced clear post-depositional downward tilting towards the diapir, as revealed by (Fig. 5): (1) clear progressive downward bending of units 5 and 6 towards the valley margin; (2) re-oriented fabrics in the colluvial units 3 and 7, with the major axis of the clasts showing persistent anomalous dips into the slope; and (3) planar base of the wedge-shaped colluvial unit 7 dipping into the slope. It can be confidently assumed that the layers of fine-grained alluvial facies were deposited subhorizontally, and that the large clasts in the colluvial deposits used to have a dominant downslope dip roughly concordant with the former slope. The channel represented by unit 4 indicates a paleotopography in which the lowest part of the valley was located in the valley axis. However, the sediments accumulated at the valley margin next to the diapior during and after the channel fill are currently at a lower elevation, demonstrating their downward bending. The top of unit 5 and the base of unit 6 indicate a minimum vertical drop within the trench of 85 cm. This vertical displacement, together with the age of 1716-1570 cal yr BP obtained for unit 5, indicates a minimum local subsidence rate of 0.5 mm/yr. Similarly, the dip of 19° of unit 6 at the SE edge of the trench indicates a minimum rotation rate of around 12°/kyr. The actual values can be significantly higher, since the trench has only exposed part of the bending structure. The exposed deformation suggests that the late Holocene deposits associated with the edge of the salt extrusion are affected by a synformal structure, which outer limb was exposed in the trench. This interpretation is supported by synformal geometries captured in this zone by the ERI and SR sections (Fig. 2).

4.3. Northern lacustrine synkinematic sequence

This exposure is located on the northeastern slope of the Salt Mountain, where the salt bedrock is covered by a flap of upturned Quaternary deposits (labelled as 2 in Fig. 3). Here, the top and flank of the protruding salt extrusion are draped by folded colluvium with large angular sandstone cobbles and boulders sourced from the sandstone slopes to the NW (Fig. 6). The fold in the colluvium seems to correspond to the upper bend of a monocline with a steeply dipping to vertical intermediate limb and a lower hinge at the margin of the extrusion, buried beneath the peripheral depression. This colluvial deposit shows an elevation difference of 38 m between the top of the Salt Mountain and its topographically lowest exposure at the margin of the peripheral depressions, providing a minimum measure for its diapiric uplift. The actual value can be considerably higher because: (1) the topographically lower part of the colluvium is not exposed; and (2) the colluvium was deposited with a primary inclination towards the diapir. Around 400 m to the SW, the base of the colluvial deposits has been roughly situated in the ERI section 25 m below the floor of the depression (Fig. 4), suggesting a vertical diapiric uplift for this unit of around 63 m.

At the lower part of the slope and at the margin of the peripheral depression, a rotated lacustrine succession dipping away from the diapir unconformably overlies and abuts the folded colluvium (Fig. 6). Wagner et al. (1971) found in these deposits plant remains, charophytes, gastropods, and ostracoda (*Limnocythere* sp., *Cyprideis* sp.) characteristic of mesohaline environments. The logged lake deposits reach 14.2 m in thickness (Column N in Fig. 7). The lowermost section, less than 5 m thick, could not be exposed due to access limitations. The lacustrine succession mainly consists of well-bedded layers of centimeter-scale thickness with planar and parallel stratification. The lacustrine facies

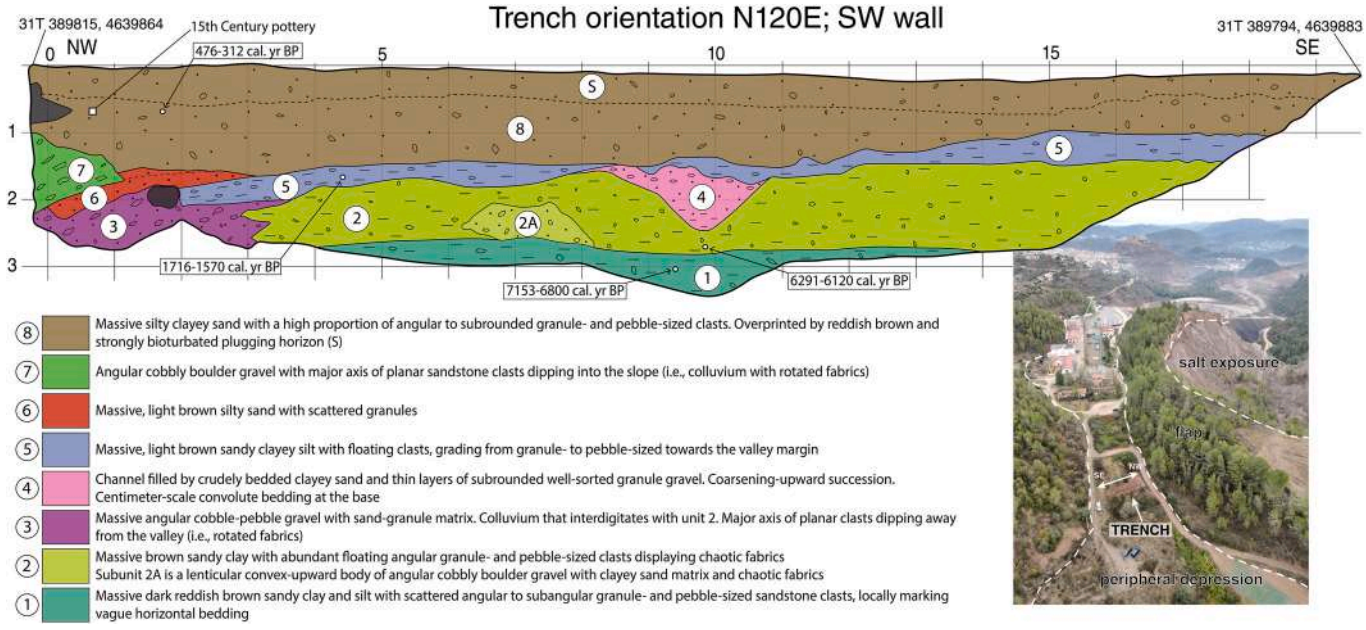

Fig. 5. Log of trench excavated in the peripheral depression adjacent to the rising salt extrusion covered by a flap of colluvial deposits. Note Holocene alluvium and colluvium with rotated fabrics dipping towards the diapir on the NW sector of the trench. Pottery fragment determined by Dr. Xavier Rocas, curator of the Terracotta Museum, La Bisbal d'Empordà.

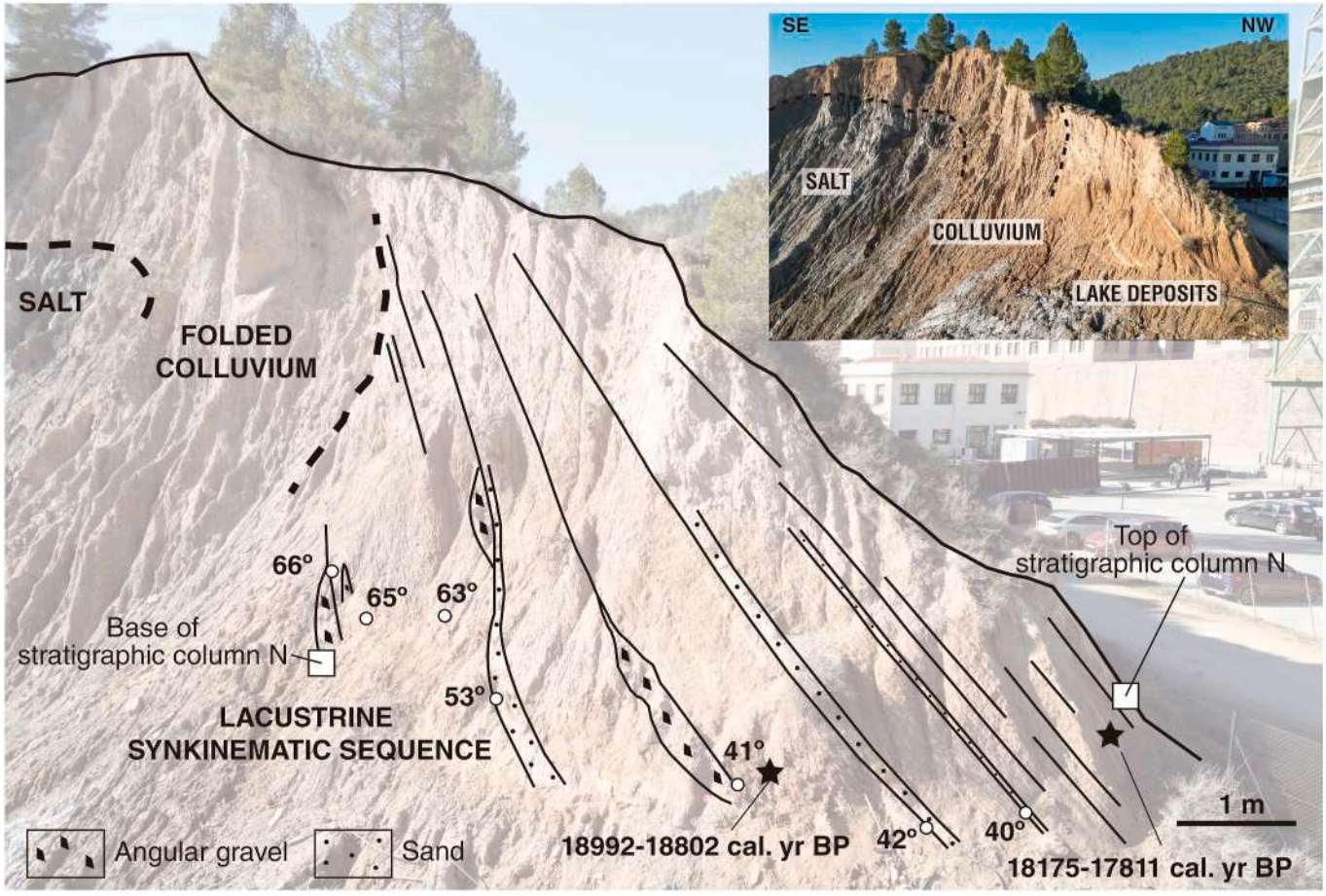

Fig. 6. Annotated images of the late Pleistocene lacustrine synkinematic sequence exposed on the northern flank of the Salt Mountain and at the margin of the peripheral depression (location labelled as 2 in Fig. 3). The lake deposits with growth stratal geometry unconformably overlie folded coluvial deposits that drape the top and flank of the salt extrusion.

include, in order of importance: Cm (53%, beds up to 69 cm thick): massive reddish brown silty clay; Cl (21%, beds up to 30 cm thick): laminated reddish brown clay with gastropods; Ml (2.5%, beds up to 6 cm thick): laminated green and reddish brown clay-rich marl; and Mm (1%, beds up to 6 cm thick): massive and bioturbated greenish beige clay-rich marl. The lake deposits are locally interbedded by coarser detrital facies related to higher energy flow events, including: S (13%, beds up to 45 cm thick): Massive tabular beds of light brown clayey silty sand with fining upwards grading; and G (9.5%, bed up to 65 cm thick): massive angular pebble-cobble gravel of sandstone clasts filling ribbon- and sheet-like channels with irregular erosional base. The proportion of the laminated clay and marl facies (Cl, Ml) shows a general increase towards the top of the exposed succession indicating a deepening trend.

The lacustrine deposits display growth stratal geometry (cumulative wedge out) indicative of deposition coeval to diapiric rise (synkinematic sequence). The sedimentary packages thin towards the diapir and the strata show upward dip attenuation, from around 65 to 40° (Fig. 6). A significantly higher dip can be expected for the lowermost unexposed section juxtaposed to the colluvial unit. Two samples of gastropods obtained from laminated clays (facies Cl) at 8.75 and 12.1 m above the base of the logged succession yielded radiocarbon ages of 18,992–18,802 cal yr BP and 18,175–17,811 cal yr BP, respectively. A Plio-Quaternary (Villafrachian) age was previously suggested for these deposits, based on their intense deformation and relative elevation with respect to the Cardener River (Riba et al., 1975). The obtained age ranges and the thickness between the sampled beds (3.35 m) indicate a rough average aggradation rate of 2.8–5.3 mm/yr. These beds dated at ca. 19-18 ka dip around 40°, indicating an average rotation rate of 2.1–2.2°/kyr. Note that this rate refers to the specific point where the dip was measured, and that it can vary significantly across the flap. Additionally, the estimated elevation difference of the colluvial unit (63 m) and the available minimum age given by the overlying lacustrine succession (ca. 18–19 ka) indicates a long-term uplift rate of <3.3–3.5 mm/yr.

4.4. Southern lacustrine synkinematic sequence

This lacustrine sequence is exposed along 200 m in a NE-SW-oriented ridge associated with the southeastern edge of the salt extrusion (the Salt Mountain) (labelled as 3 in Fig. 3). The ridge corresponds to the erosional remnant of a flap of late Quaternary deposits situated on the SE edge of the Bofia Gran karst depression, and below a steep slope ca. 100 m high underlain the Suria Formation (Fig. 8). Stratigraphic logs have been constructed in the main exposures (Fig. 7).

The section corresponding to Column S1 occurs on the NW-facing slope of the ridge (Fig. 8B). It shows a succession 14.1 m thick of lacustrine sediments steeply dipping away from the diapir and overlying colluvial deposits. These are the oldest exposed deposits of the lacustrine succession, showing distinctive beds of greenish massive and laminated marls in the lower part (labelled as marker beds in Fig. 8). A charcoal sample collected 5.4 m above the base has yielded an age of 14787-14089 cal yr BP (Fig. 7). The strata in this exposure show a cumulative wedge out arrangement (growth strata), with upward dip attenuation (85-30°) and rapid thickening of sedimentary packages away from the diapir. The beds in the lower part of the section display a sharp downward bend well-defined hinge zone. Here, there are some subhorizontal

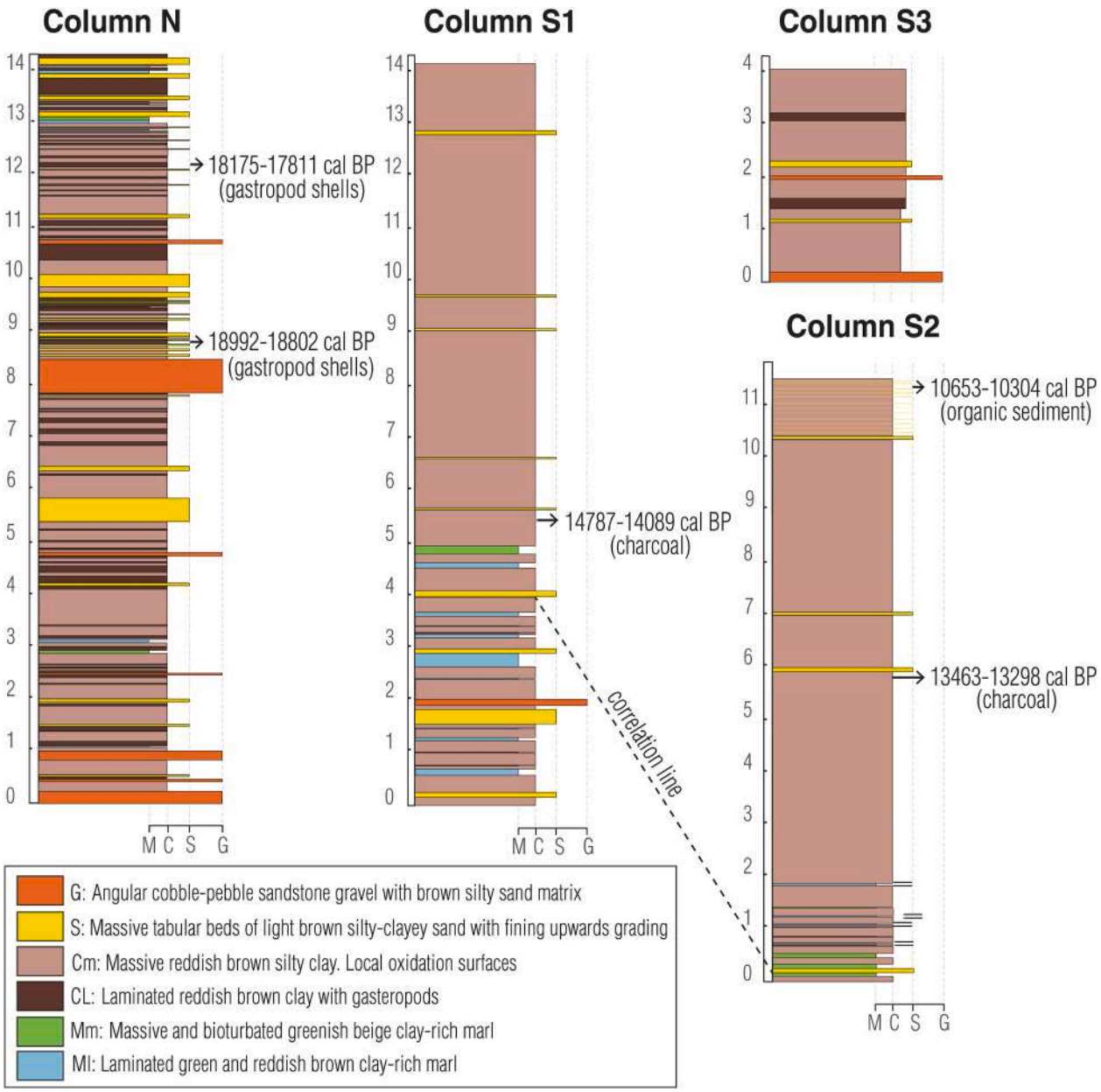

Fig. 7. Stratigraphic columns of the lacustrine synkinematic successions on the northern (Column N) and southern (Columns Sx) flanks of the Salt Mountain. The location of columns is indicated in Figs. 6, 8 and 9. Column S3 corresponds to the exposure shown in Fig. 9B. The calibrated radiocarbon ages obtained from charcoal, gastropod shells and organic sediment are indicated.

thrust faults verging away from the diapir. These faults most probably correspond to former steeply dipping reverse faults rotated by salt rise (Fig. 9A).

The exposure of Column S2 (11.5 m thick) occurs in the upper part of the NW-facing slope of the ridge and can be confidently correlated with Column S1 using the distinctive and laterally continuous beds of greenish marls and associated sands (Figs. 7 and 8B). Samples collected at 5.8 and 11.3 m above the base of this section have provided radiocarbon ages of 13463-13298 and 10653-10304 cal yr BP, respectively. The latter, derived from organic sediment, is considered less robust than the former, obtained from detrital charcoal. In this exposure the beds also display a SW-verging asymmetric antiformal bend with a gentle upper limb (30SE) and a nearly vertical lower limb. The correlated columns S1 and S2 show an aggregate thickness of 15 m. The two ages from column S2, separated 5.5 m, suggest a mean aggradation rate of 1.8–1.9 mm/yr.

The exposure of Column S3 (4.05 m thick), located in the gully excavated between the sandstone slope and the ridge formed by the flap of deformed Quaternary deposits, displays the youngest preserved lacustrine sediments (Figs. 7 and 9B). Here, the strata show a SE-facing monocline with interlimb angle of 90° (i.e. knee bend) with dips abruptly changing in the hinge zone from horizontal to vertical in the upturned limb. A few meters further to the NE, it can be observed that the deposits of the horizontal limb are underlain by sandstone dipping away from the diapir. This abrupt hinge zone seems to be controlled by the boundary between the mobile salt and the quasi-static country rock.

The integration of the data obtained from the different outcrops indicate that the lacustrine synkinematic sequence has a minimum thickness of around 20 m, recording deposition over more than 5 kyr in an enclosed or poorly drained elongated depression at the margin of the diapir. The development of this lacustrine environment is most likely related to the damming of the peripheral drainage by extruding salt. The

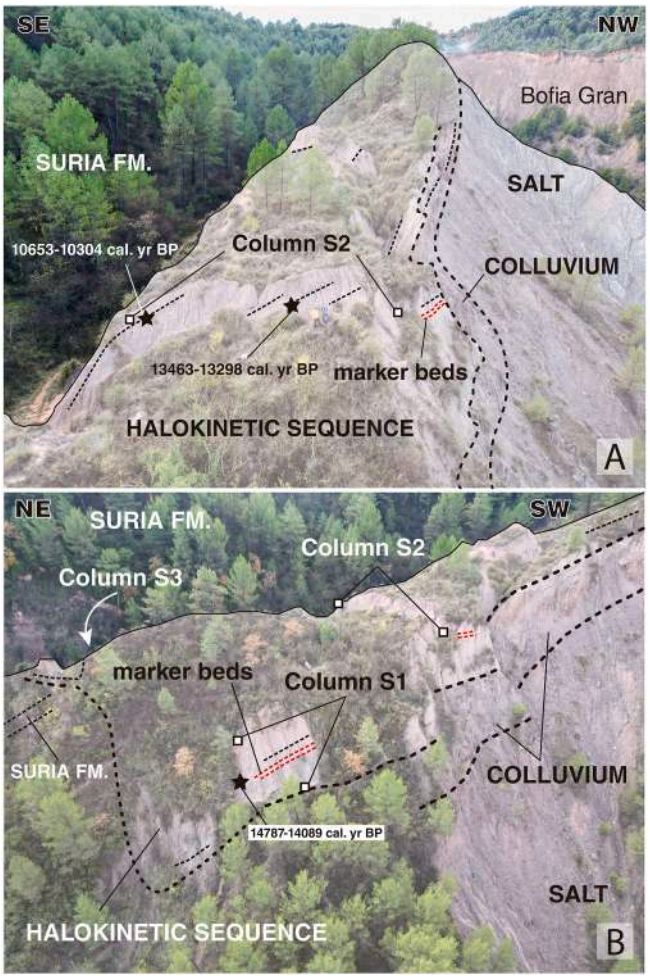

Fig. 8. General views of the southern lacustrine sequence indicating the location of the analyzed exposures, the stratigraphic columns, and radiocarbon ages (site labelled as 3 in Fig. 3). These late Quaternary deposits correspond to the erosional remnant of a flap abutting the salt extrusion and situated at the foot of a steep and high-relief slope underlain by the Suria Fm. A: Longitudinal view showing the location of Column S2. B: Transverse view indicating columns S1 and S2, correlated using the marker beds. Note horizontal attitude of the lacustrine deposits overlying sandstone of the Suria Fm. on the left.

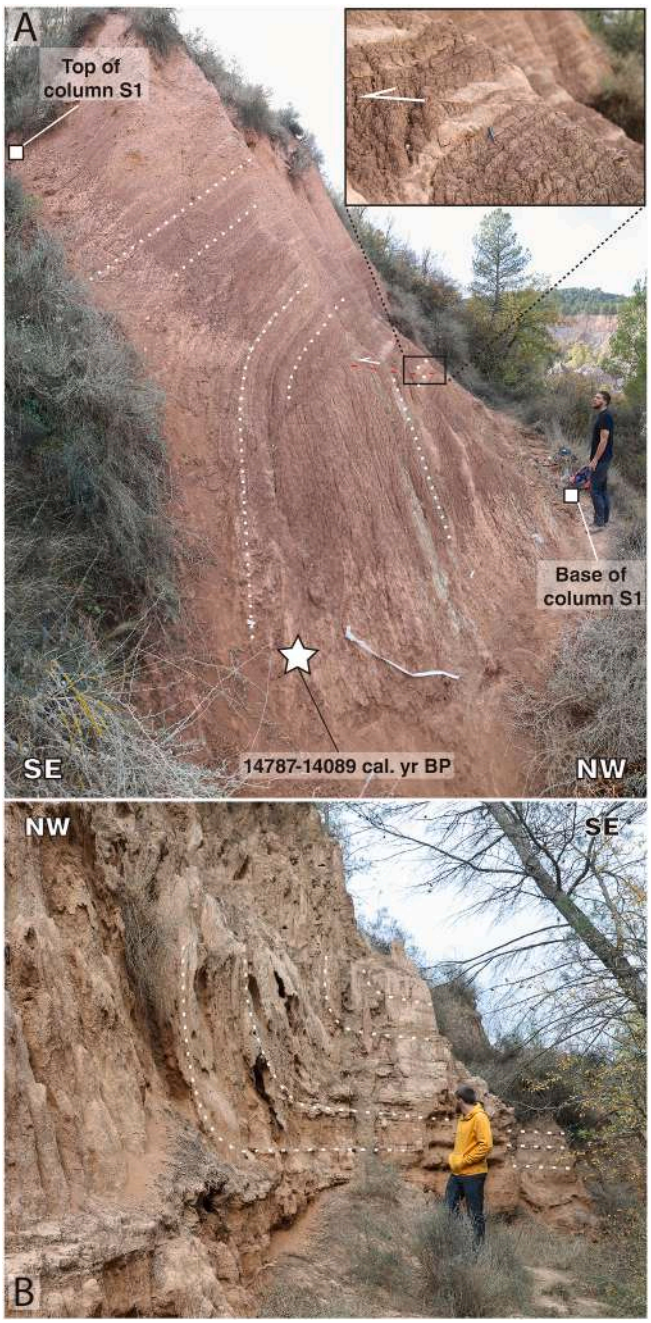

Fig. 9. Outcrops of the southern lacustrine sequence. A: Exposure of the lower section of the lacustrine deposits dipping away from the diapir, showing an asymmetric SE-verging bend with growth stratal geometry and small-offset reverse faults (rotated) in the hinge zone. B: Outcrop of the youngest preserved lacustrine deposits located in the gully situated at the foot of the slope of Suria sandstone. Beds display a monocline facing away from the diapir with vertical dip in the upper limb and horizontal beds in the lower limb underlain by Suria sandstone (observable a few meters downstream).

overall internal structure of the succession corresponds to a monocline with the axial trace of the lower hinge dipping towards the diapir (Fig. 10). The stratigraphic units show and outward-migrating monoclinal front and a basal synform onlapping onto the bedrock. This arrangement is consistent with deposition in a wedge-shaped trough (thinner in the diapir side) flanked by: (1) a rising salt extrusion that tends to displace the basin upwards and laterally away from the diapir; and (2) a steep erosional antidip slope in the country rock that acts as a lateral confinement for deposition. The progressive differential uplift and outward rotation of the diapir caused the monoclinal folding and contraction of the sedimentary fill, with the confining margin on the country rock acting as a backstop.

4.5. Southern late holocene valley fill

This synkinematic succession is associated with the SE edge of the salt extrusion at the margin of the Southern Valley (labelled as 4 in Fig. 3). Here, there is a salt hill capped by a differentially uplifted colluvial deposit forming a backtilted top surface (Fig. 11). It can be inferred that the colluvium, with an original slope towards the valley, has been upturned to form a monoclinal drape fold with a buried lower bend. An exposure on the SW face of the hill shows a valley fill nested in the lower flexure of the monocline, overlying and abutting the folded colluvium. The alluvial deposit, with an exposed thickness of around 5 m, shows growth stratal geometry indicative of sedimentation coeval to ground deformation. The following facies have been identified in this synkinematic valley fill: S–C: fining-upwards couplets of sand and silt; Sm: massive sand with granules; Sh: laminated sand with granules; Fm: massive silt with floating angular gravel; Bm: massive, poorly sorted, angular pebble-cobble gravel with chaotic fabrics. Facies S–C, Sm and Sh

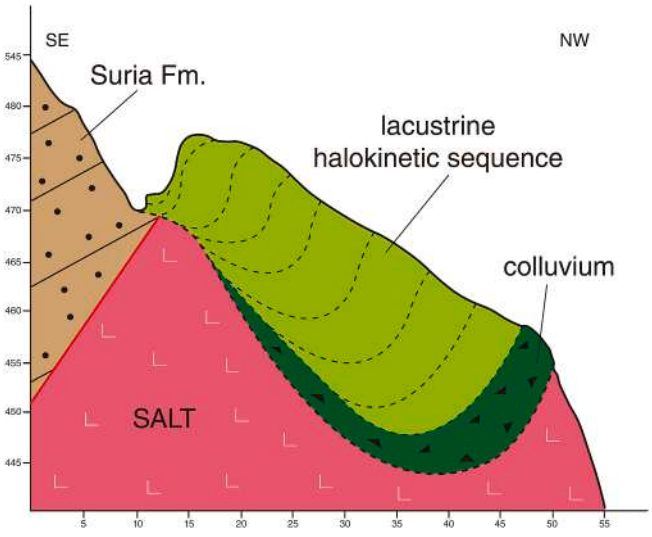

Fig. 10. Schematic cross-section of the late Quaternary lacustrine sequence with an overall monoclinal structure preserved on the SE edge of the diapir. The arrangement of the deposits with a basal onlap records the upward and outward displacement of the basin towards the diapir margin, where the steep slope on Suria Fm. functioned as a lateral confinement for deposition and a backstop for deformation.

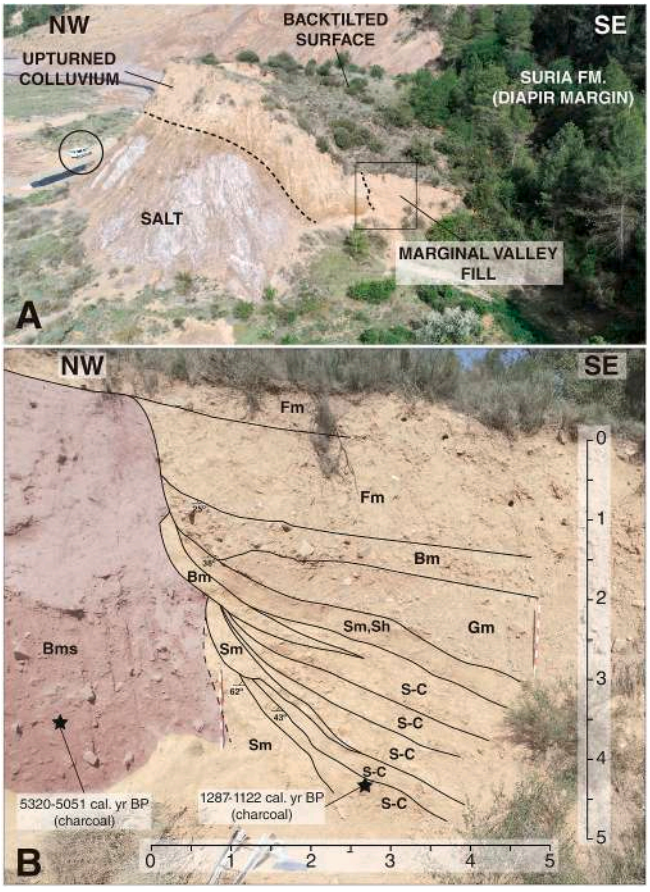

Fig. 11. The southern late Holocene valley fill. A: General view of the salt hill covered by a differentially uplifted colluvium with a backtilted top surface. The rectangle indicates the area show in B. B: Outcrop showing a halokinetic valley fill abutting and overlying the upturned colluvium. See description of lithofacies codes in the text.

are interpreted as fluvial channel deposits, whereas Fm and Bm as reworked slope deposits transported by slope wash and channelized flows, respectively.

The strata in the valley fill display cumulative wedge out arrangement, with bed thickening away for the diapir and dips increasing downwards and laterally towards the diapir (Fig. 11). It can be interpreted that differential halokinetic uplift generated a trough along the edge of the salt extrusion controlling a longitudinal drainage confined between a backtilting surface and the marginal slope on Suria sandstone. The valley was filled synkinematically until the drainage was re-routed either by fluvial erosion or captured by a swallow hole. A charcoal sample collected from a bed of facies S–C has yielded a radiocarbon age of 1287-1122 cal yr BP. This layer, which can be assumed to be deposited with a subhorizontal attitude, currently dips 43°, indicating a rotation rate of 33–38°/kyr. This rotated unit shows a minimum vertical displacement in the exposure of 2.5 m, yielding a minimum vertical displacement rate of 1.9–2.2 mm/yr. The adjacent and underlying colluvial deposit has been dated with charcoal at 5320-5051 cal yr BP. The differential uplift of 19 m observable at the exposure, together with the numerical age indicate a minimum vertical displacement rate of 3.6–3.8 mm/yr. The actual value can be much higher, since the upturned deposit may have been significantly eroded on its distal sector and may be situated a significant depth below the valley fill.

4.6. Strath terraces of the Cardener River

This site is located on the west margin of the Cardener River valley excavated across the northern limb of the Cardona Anticline and its salt core (labelled as 8 in Fig. 3). Here, a steep salt slope on the outer side of a meander displays three stepped strath terraces with planar geometry cut across the rising salt (Fig. 12). These rock-cut surfaces are overlain by inset fluvial deposits capped by colluvium. The fluvial deposits up to 7 m thick mainly consist of well-sorted, fine-grained facies (i.e., massive and laminated sands and muds). They typically display an indurated white crust of salt attributable to evaporative precipitation of halite from brines rising by capillarity. The strath surfaces and the overlying fluvial deposits show clear upstream tilting related to differential uplift, with the amount of uplift decreasing towards the edge of the extrusion. The amount of rotation increases with the age of the surface, with apparent dips of 6° and 11° in the intermediate and upper salt-cut straths, respectively.

The radiocarbon ages obtained from the fluvial deposits can be used to assess local rates of halokinetic uplift, considering that the Cardener River has maintained a graded profile in the investigated site and that the long-term incision rate of the fluvial system (ca. 0.3–0.5 mm/yr; Luque and Julià, 2007) is much lower than halokinetic uplift. This perennial fluvial system can rapidly adjust its longitudinal profile across the rising diapir (i.e., dynamic equilibrium), given the high solubility of the salt (De Waele and Gutiérrez, 2022). The possibility of the fine-grained fluvial facies being high-stage flood deposits (i.e., deposited well above the base level) can be ruled out given the broad geometry of the valley. A charcoal sample collected 0.4 m above the lower strath and situated at 10.27 m above the thalweg has yielded an age of 728-664 cal. yr. BP (Fig. 12). These values indicate an average uplift rate of 12.8–13.9 mm/yr (12.3–13.4 mm/yr considering the relative height of the strath). Given the young age of the deposits, these rates and the following ones are calculated considering years before 2023 (i.e., adding 73 years to the BP ages). Detrital charcoal obtained 0.2 m above the intermediate strath and lying 20.79 m above the channel has been dated at 1248-1058 cal yr BP, indicating an uplift rate of 15.8–18.4 mm/yr (15.6–18.2 mm/yr considering the relative height of the strath). At the confluence zone between the Cardener River and the Northern Valley, the intermediate strath is overlain by a fluvial succession around 7 m thick with interfingered deposits attributable to both drainages (coarser and less sorted from the tributary). Charcoal obtained from a gravelly sand bed situated 6 m above the intermediate strath has been dated at

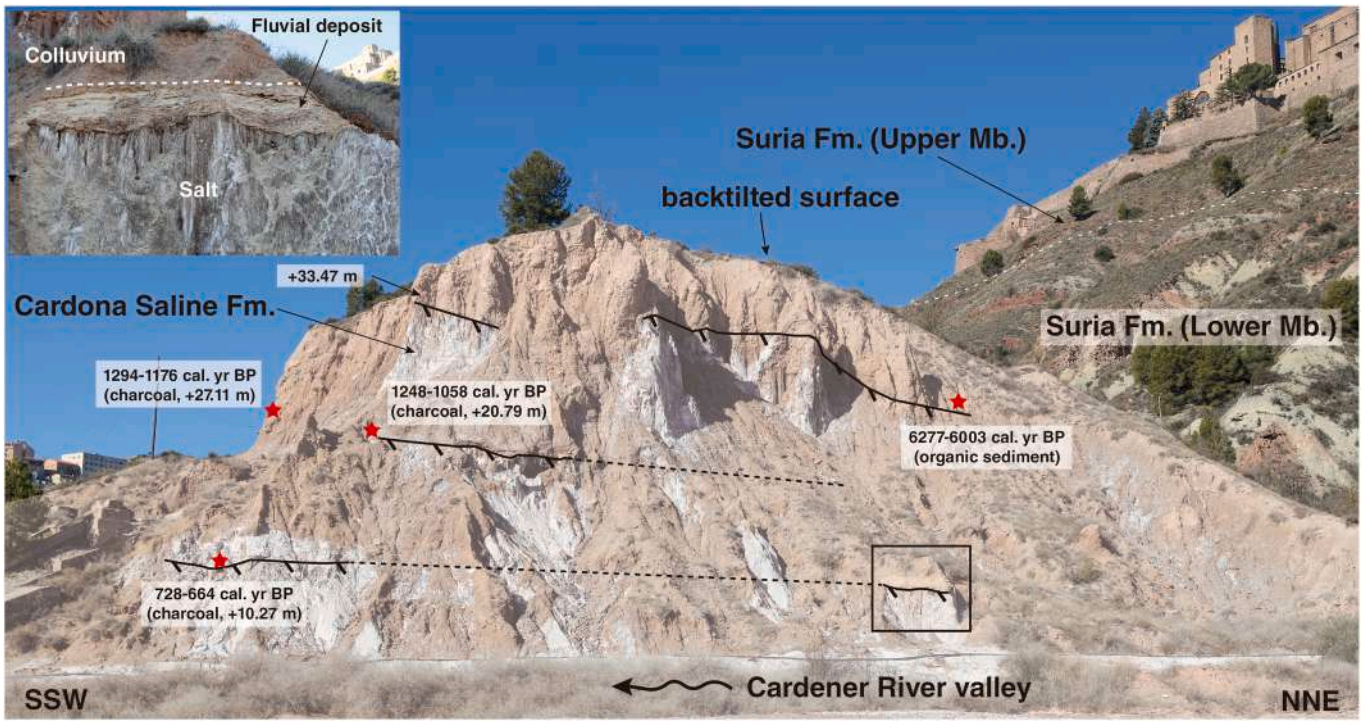

Fig. 12. Uplifted and tilted strath surfaces cut into salt and covered by a thin veneer of alluvium on the western margin of the Cardener River valley. Labels indicate radiocarbon ages and relative heights measured with DGPS. Note higher amount of tilting in the older surfaces. The square indicates area covered by the inset image of the lower salt-cut strath.

1294-1176 cal yr BP. The similar ages obtained from the samples collected 0.2 and 6 m above the strath suggest that aggradation of the 7 m thick fluvial succession occurred in a short period of time. Consequently, the upper sample may provide a supra-elevated record for the paleobase level and a maximum uplift rate. Two alternative uplift rates can be calculated with the relative height of the sampled bed (27,11 m; maximum uplift) and that of the strath (20.79 m; best approximation for uplift), yielding values of 19.8–21.7 mm/yr and 15.4–16.9 mm/yr, respectively. Both rates compare well with the ones computed with the previous samples. An attempt was made to date the upper strath terrace with organic-rich mud situated at 0.2 m above the base of the fluvial deposit. However, the obtained age of 6277-6003 cal yr BP from organic sediment is not considered to render a valid age estimate. This age, and the relative height of the strath at its upper part (33.40 m) would indicate a non-consistent uplift rate of 5.3–5.6 mm/yr.

4.7. Strath terraces of the southern valley

The salt slopes on both margins of the Southern Valley display laterally continuous rock strath surfaces overlain by fluvial deposits. These terraces represent markers of paleobase-levels (i.e., valley floor) uplifted and perched by diapiric rise and concomitant fluvial incision (Fig. 13). The fluvial deposits, inset into the salt bedrock and often overlain by colluvium, typically consist of well-bedded and well-sorted sand, mud and granule gravel. At some sites, the alluvium fill subhorizontal notches a few tens of centimeters high carved by lateral solutional undercutting (Fig. 13A). The salt slope of the hill with backtilted top surface (labelled as 4 in Fig. 3) displays two laterally continuous remnants of strath surfaces expressed alluvium-filled notches. Remains of plant leaves from the upper level, situated at 27.55 m above the current base level and 0.25 m above the strath, have been dated at

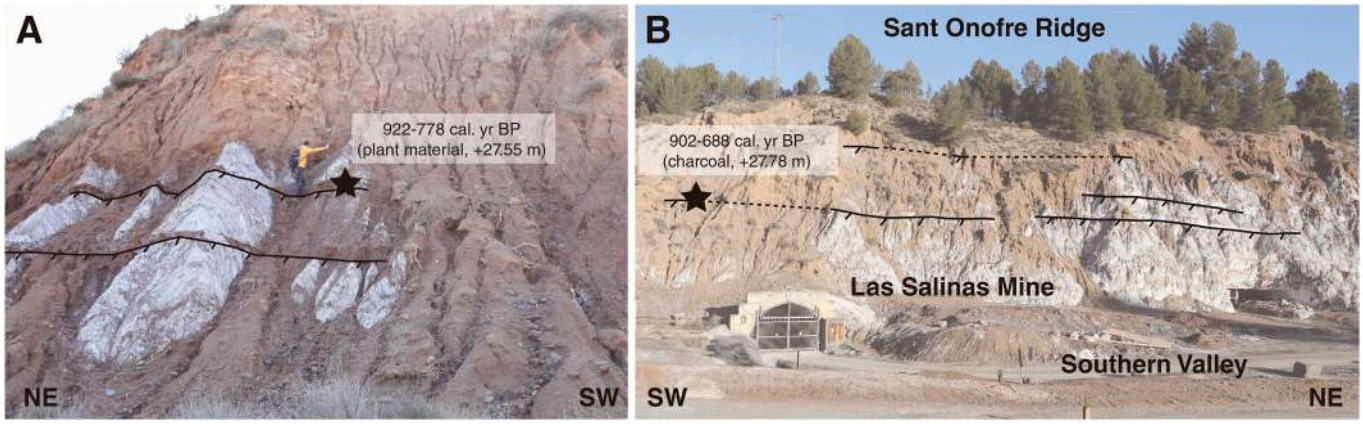

Fig. 13. Salt-cut strath surfaces with fluvial deposits in the Southern Valley. A: Two straths corresponding to laterally continuous alluvium-filled notches generated by lateral solutional undercutting. Person with DGPS on the upper strath dated with plant material (point 4 in Fig. 3). B: Three straths on the SE-facing salt slope of the Sant Onofre Ridge (point 6 in Fig. 3). The lower was dated with detrital charcoal.

922-778 cal yr BP, yielding an uplift rate of 32.4–27.7 mm/yr (32.1–27.4 mm/yr considering the relative height of the strath). This rate and the following ones are calculated considering years before 2023. In the vicinity of Las Salinas Mine, the slopes of the Sant Onofre Ridge on the NE margin of the valley show three strath surfaces with thin veneers of fluvial deposits (labelled as 6 in Fig. 3). A charcoal sample from the lower one, lying 27.78 m above the valley floor and 0.45 m above the strath, has been dated at 688–902 cal yr BP, proving an uplift rate of 36.5–28.5 mm/yr (35.9–28.0 mm/yr considering the strath height), very similar to the previous one. Further downstream, the salt bedrock in a hill with backtilted surface on the SE valley margin (labelled as 7 in Fig. 3) is carved by a strath terrace at a relative height of 16.25 m. Detrital charcoal from the overlying fluvial deposit (0.15 m above the base) has provided an age of 1271-1070 cal yr BP. These values indicate a mean uplift rate of 14.2–12.1 mm/yr (14.1–12.0 mm/yr considering the strath height). This rate estimate is about half of the previous ones.

5. Discussion

The Cardona-Pinós salt anticline is a detachment fold in the southern foreland of the Pyrenees (Ebro Basin) developed in late Eocene-Miocene times by regional shortening (Fig. 1). Buckle folding was accompanied by salt flow from the synclines towards the low pressure core of the anticlines. Syntectonic sedimentation coeval to fold growth resulted in a supra-salt overburden with significant thickness variations across the folds. In the anticline crests the overburden is significantly thinner and the salt is closer to the surface (Fig. 3). At some stage after the capture of the endorheic Ebro Basin, erosion of the thinned overburden in the anticline lead to the emergence of the salt and the post-shortening development of the Cardona salt extrusion, spatially associated with the deeply entrenched Cardener River valley. The driving mechanism and timing for the initiation of the Cardona Diapir was investigated by Sans and Koyi, 2001 by means of a scaled analogue model and numerical calculations. These authors proposed that salt extrusion was initiated by piercement of the overburden in the anticline crest thinned by even erosional lowering up to a critical thickness. We concur that erosion is the main driving mechanism for the development of the Cardona salt extrusion. However, based on the long-term evolution of the landscape and field evidence, we propose that localized erosional unroofing by fluvial entrenchment, rather than erosion-induced piercement, was the main process responsible for the inception of the Cardona Diapir.

In the centrifuge model by Sans and Koyi, 2001, the analogue for salt (silicone putty) and overburden (microlaminites of plasticine and Dow Corning silicone) were initially shortened by 12% to produce open detachment folds. In a subsequent step, the effect of erosion on the Cardona Diapir was simulated by evenly removing around 80% of the thickness of the folded overburden to create a horizontal erosional surface cut across the folds. The centrifuge run of the “eroded model” produced elongated diapirs (salt walls) and extrusions along the crest of the anticlines. Based on this model results, Sans and Koyi, 2001 ascribed the development of the Cardona Diapir to: (1) salt flow from the areas of thicker overburden (synclines) towards areas of thinner overburden (erosionally unroofed anticlines); and (2) piercing of the overburden in the anticline crests. They calculated a piercing critical thickness of 300 m for the Cardona Diapir considering the driving force related to differential loading and the resisting force given by the shear strength of inward dipping crestal faults with a high coefficient of friction of 0.85. Additionally, they estimated that the onset of piercing occurred at around 2 Ma assuming: (1) that the removal of an overburden thickness of 2.2 km for the crest of the Cardona-Pinós Anticline; and (2) a constant and spatially uniform erosional lowering rate of 15 cm/yr (which is exceptionally high), that started at ca. 14.5 Ma when supposedly the basin became exorheic.

The erosional style conceived by Sans and Koyi, 2001 in their models, whereby the ground surface experiences an even lowering, does not properly account for the geomorphic evolution of the region. Here, erosion is dominated by fluvial incision governed by the discordant Cardener River (i.e., base level), which traverses perpendicularly the Cardona-Pinós Anticline (Figs. 1 and 3). Most probably, the entrenchment of the Cardener River locally breached the overburden in the anticline crest leading to the break out and spelling of the salt. The erosion of the overburden and the expansion of the salt extrusion propagated along the anticline axis to the SW, controlled by the NE plunge of the fold at the site, resulting in an elongated passive diapir (salt wall) located in the floor and SW margin of the Cardener River (Fig. 3). This implies a progressively more youthful extrusion towards the SW, in agreement with geomorphic evidence, showing a less dissected and degraded domal morphology in the Salt Mountain (Fig. 2). Geochronological information on Quaternary fluvial incision in the NE sector of the Ebro Basin is rather limited compared with other sectors of the basin (e.g., Benito-Calvo et al., 2022). Nonetheless, calcareous tufa terraces of the Llobregat River, lying at 85–90 m and 55–65 m above the channel and situated 45 km downstream of Cardona (see location in Fig. 1), have been dated by U/Th at ~350 ka and 111 ka (Luque and Julià, 2007), indicating a long-term incision rate of 0.3–0.5 mm/yr. Assuming a similar incision rate for the Cardener River at Cardona, these values indicate that fluvial entrenchment can locally remove as much as 100 m of overburden in a time span of around 200–330 kyr. This erosional style and the incision rate strongly suggest that the timing of the initiation of the Cardona salt extrusion is much younger than the 2 Ma proposed by Sans and Koyi, 2001, as supported by the numerous radiocarbon ages obtained from deposits associated with the salt diapir in this work (Table 2). Additionally, the overburden piercement preceding the extrusion suggested by Sans and Koyi, 2001 is difficult to conciliate with field data, given the lack of evidence of active deformation along the crest of the anticlines with overburden thickness below the calculated critical value of 300 m (e.g., crestal faulting). Sans and Koyi, 2001 predicted that piercement in the Suria Anticline, with an estimated critical overburden thickness of 200 m, will start in 2–3 Myr. However, the Cardener River is already entrenched into the salt core of the Suria Anticline (i.e., floodplain alluvium underlain by salt; Valle de Lersundi, 1999; Institut Cartogràfic i Geològic de Catalunya, pers. comm). The erosional unroofing model proposed here, dominated by localized fluvial entrenchment rather than uniform erosional lowering, involves that there may exist differential loading not only between the synclines and the anticlines (overbudern loading), but also between the valley margins and the valley floor (topographic loading), with a local relief or around 200 m. Gutiérrez et al. (2019) review a number of case studies in which halokinetic activity (i.e., gravitationally-driven salt flow) is initiated or enhanced by fluvial incision.

The data gathered in the Cardona salt extrusion by detailed mapping, outcrop analysis, geophysics, trenching and radiocarbon dating of 18 samples allow gaining insight into a number of poorly explored aspects: (1) Geomorphic evolution of a salt extrusion and morpho-sedimentary environments created by passive diapirism in an erosional continental environment. Most works that address the impact of passive diapirm on sedimentation deal with salt structures located in the aggradational floor of actively subsiding basins (e.g., Giles and Rowan, 2012; Jackson and Hudec, 2017). (2) Morpho-stratigraphic arrangement and deformation style of recent deposits associated with a salt extrusion essentially unaffected by any significant regional stress (i.e., halokinesis driven by overburden loading). Distinguishing between deformation caused by passive diapirism and regional tectonics in sediments adjacent to diapirs is often a challenging issue (Rowan et al., 2020). (3) Geochronology of late Quaternary deposits deformed by halokinesis and long-term rates of ground displacement by passive diapirism. This is a poorly explored topic with important practical implications (e.g., mining, storage of resources and waste disposal, hydrocarbon exploration, feasibility of engineering projects).

The geomorphic and stratigraphic relationships observed in the Cardona salt extrusion reveal a general temporal trend involving relief

inversion related to salt rise and the formation of marginal depressions (Fig. 4). These marginal troughs eventually host lacustrine and fluvial environments confined between the rising salt and the steep slopes on the country rock. In contrast, sedimentation associated with steep passive diapirs (salt stocks, salt walls) in the floor of sedimentary basins commonly lack any external lateral confinement. In the initial stages following the erosional exposure of the salt, the rising diapir was buried by rapid deposition of coarse-grained colluvium sourced from the marginal sandstone slopes and mainly deposited by mass wasting processes (debris flows, shallow landslides). The wedge-shaped colluvial deposits were differentially uplifted by drape monoclinal folding to form upturned flaps, resulting in relief inversion, whereby deposits accumulated in a low-lying area rise to a prominent position. The uplift and outward rotation of the flaps, which locally protect the salt from dissolution, result in the development of salt-edge depressions between backtilting surfaces and the country-rock slopes (Fig. 14). These marginal troughs eventually hosted lake environments (late Pleistocene lacustrine sequences at sites 2, 3 in Fig. 1) and controlled the development of marginal longitudinal drainages (late Holocene fluvial deposits at sites 1, 3 in Fig. 1), both with deposition of halokinetic growth strata (Figs. 6, 8 and 11). The formation of internally or poorly drained salt-edge lacustrine systems was probably induced by the blockage of the marginal drainage by the lateral expansion of the salt extrusion and/or landsliding. In contrast with the colluvial facies, deposition of the lacustrine and fluvial deposits was essentially restricted to the edge of the diapir, indicating low sedimentation rate compared with the rate of diapir rise (Fig. 14). The occurrence of a ridge capped by colluvium along the axis of the salt wall (Sant Onofre Ridge) flanked by two longitudinal drainages (Northern and Southern Valleys) suggests another case of relief inversion, whereby the drainage was displaced laterally away from the more rapidly rising axial sector of the salt wall (Fig. 3).

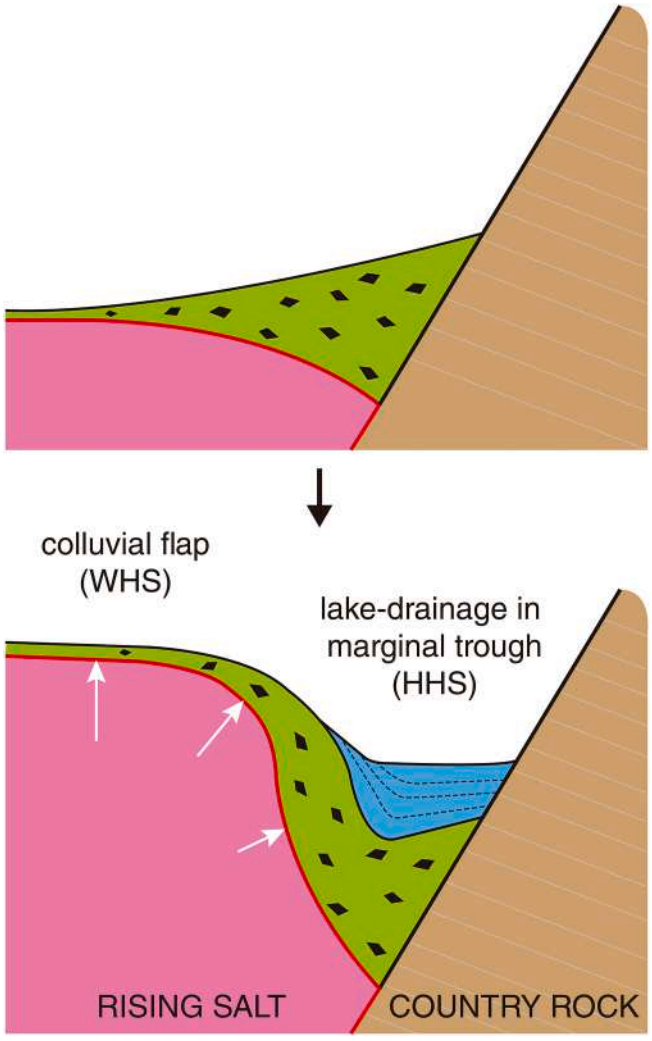

Fig. 14. Sketch illustrating the morpho-sedimentary evolution of the flank of the salt extrusion, involving relief inversion. Initially, rapidly depositing colluvium onlaps and encroaches the rising salt. In a subsequent stage, the uplift and outward rotation of the colluvium creates a marginal trough between the drape folded colluvial flap and the country rock slope. Lake environments or a marginal longitudinal drainage eventually form along the salt edge. These two morpho-sedimentary units can be ascribed to a wedge halokinetic sequence (WHS) and a hook halokinetic sequence (HHS), characterized by ratios between diapir rise rate and sedimentation rate lower and greater than 1, respectively.

The deformation of the analyzed diapir-flanking deposits is dominated by drape monoclinal folding with very limited faulting, as is commonly the case in synkinematic sediments adjacent to passive diapirs (Rowan et al., 2020). The well-stratified lacustrine and fluvial deposits display halokinetic growth strata with bed thinning towards the diapir and both upward and outward dip attenuation (Figs. 6 and 11). The geometric relationships observed in the southern lacustrine halokinetic sequence, deposited in a trough confined between the mobile diapir and the static country rock slope, indicate that salt rise and flap rotation induced the upward and outward migration of the depositional axis. Here, the country-rock slope functioned as a lateral backstop for deformation, probably contributing to some shortening in the trough fill with an inferred basal synformal structure (Fig. 10) and observed reverse faulting (Fig. 9A).

The trench excavated across the peripheral depression adjacent to the Salt Mountain exposed recent sediments (ca. 1.7–1.5 ka) with an anomalous dip towards the diapir, which probably corresponds to the limb of a synform (Fig. 5), as supported by geophysical data (Fig. 4). Several explanations can be proposed for this local structure: (1) rim syncline generated by the outward pressure of a radially expanding salt body (Stewart, 2006), which increases towards the upper part of the diapirs (Nikolinakou et al., 2014); (2) inward bending of strata over a shoulder at the edge of the diapir (Gutiérrez et al., 2019; Rowan et al., 2020 and references therein); (3) local salt dissolution and subsidence caused fresh groundwater derived from the adjacent Suria sandstone.

The two types of deformed morpho-stratigraphic units flanking the diapir can be compared with the two-end member types of halokinetic sequences described for steep passive diapirs developed in the floor of subsiding sedimentary basins (Rowan et al., 2003; Giles and Rowan, 2012) (Fig. 14). The older colluvial flaps, encroaching and onlaping the salt and recording a low diapir rise rate to sedimentation rate ratio are comparable with the wedge halokinetic sequences. In contrast, the lacustrine and fluvial deposits confined to the marginal depressions at the foot of the monoclinal scarps developed in the colluvial flaps can be ascribed to hook halokinetic sequences. These deposits thin and fold up to nearly vertical dips in short distances (Figs. 6, 8–10). The high diapir rise rate to sedimentation rate ratio that characterize these hook sequences is supported by the relatively low aggradation rates calculated with the available radiocarbon ages; 2.8–5.3 mm/yr and 1.8–1.9 mm/yr in the northern and southern lacustrine sequences, respectively. These values are one order of magnitude lower than the diapir rise rates estimated with the uplifted strath terraces. The slopes surrounding the salt extrusion may yield highly variable sediment supply depending on whether they are covered by vegetation or not. Changes in the land cover controlled by climate variability and anthropogenic factors may have played an important role in the development of the two types of Holocene halokinetic sequences.

The young radiocarbon ages obtained from deposits strongly deformed by halokinesis (uplift, rotation) reveal that the Cardona Diapir is currently experiencing vigorous salt extrusion and rise. The calculated rotation rates from dated dipping beds show significantly lower values for older deposits: (1) 2.1–2.2°/kyr in northern lacustrine sequence ca.

18 ka; (2) 4.3°/kyr in southern lacustrine sequence ca. 15 ka; (3) 12°/kyr in trench deposits ca. 1.7 ka; (4) 33–38°/ky in southern valley fill ca. 1.2 ka. This can be explained by the fact that as the diapir rises and the onlaping sediments of the flaps are shouldered aside, folding ceases or diminishes (i.e., locked folds of Rowan et al., 2020). The numerical ages from the strath terraces of the Cardener River and their relative height (Fig. 12) indicate uplift rates within the range of 21.7–12.8 mm/yr, consistent with the available DiNSAR data in this sector of the diapir (ca. 10–20 mm/yr; Rodríguez-Lloveras et al., 2020). The upstream tilting of the terraces indicates substantial differential uplift, decreasing towards the margin of the extrusion. This can be attributed to both greater flow resistance at the margin and flow convergence towards the axis of the salt wall. For instance, the dip of 6° of the intermediate terrace (Fig. 12) indicates that in around 1000 years, the amount of uplift may vary about 10 m in a distance of 100 m perpendicular to the salt edge. Higher uplift rates would be obtained if the dated uplifted markers would be located in the axial sector of the diapir. Uplift rates calculated with the strath terraces of similar ages in the Southern Valley indicate uplift rates within the range of 36.5–12.1 mm/yr (Fig. 13). The higher rates obtained in the Southern Valley compared with those of the Cardener River can be partially attributed to the more axial position of former. The apparent longitudinal variations observed between sites 4, 6 (upstream, higher rates) and 7 can be related to along strike variations in salt rise rate. This pattern has been documented in salt walls by modeling (Vendeville and Jackson, 1992) and differential uplift of terraces along the crest of the Navarrés salt wall, eastern Spain (Gutiérrez et al., 2019).

The uplift rates estimated for the Cardona salt extrusion are considerably higher than long-term rates calculated for some passive diapirs in active strike-slip and extensional environments, such as Mount Sedom in the Dead Sea (5–7 mm/yr; Weinberger et al., 2006; Frumkin, 1996) or Jabal al Salif in the Red sea (4.6 mm/yr; Davison et al., 1996). However, they are similar to the long-term uplift rates estimated for the Alaminos Canyon diapir in the Gulf of Mexico, induced by erosion unroofing in a submatine canyon (20–40 mm/yr; Martin and Bouma, 1981). Exceptionally high salt rise rates, two to three orders of magnitude higher, have been reported for some salt extrusions with extensive salt glaciers in the Zagros Mountains, where precursor salt stocks are being squeezed by rapid tectonic shortening (contractional displacement loading), such as Kuh-e-Namak (170 mm/yr; Talbot and Jarvis, 1984) or Jahani Diapir (1000–3000 mm/yr; Talbot et al., 2000). The high Holocene uplift rates estimated for the Cardona salt extrusion, unaffected by tectonic shortening, can be attributed to a number of factors: (1) the rates have been obtained at considerable distance for the diapir edge, where salt flow is decelerated by boundary resistance; (2) the Cardona salt extrusion, which inception occurred relatively recently as indicates its geomorphic setting and the obtained ages, is currently in a youthful stage and has a limited salt breakout area; (3) the Cardona Saline Formation has a yield strength, given the low proportion of impurities and the presence of potash salts (15–20%), with lower viscosity than halite (van Keken et al., 1993; Urai et al., 2008). From the applied perspective (e.g., radioactive waste storage), a diapir uplift rate of 20 mm/yr implies that a repository built at 500 m depth would rise 200 m to a depth of 300 m in a time lapse of 10 kyr. It would be desirable to obtain long-term uplift rates in other active and passive diapirs worldwide and compare them with geodetic data, to better understand the scientific and practical implication of the process.

6. Conclusions

The Cardona salt extrusion, associated with the deeply entrenched Cardener River valley, was initiated by the post-shortening erosional unroofing of the crest of the Cardona-Pinós salt anticline. The geomorphic evolution of the area and the available geochronological data on fluvial incision (Luque and Julià, 2007), in contrast with numerical model results (Sans and Koyi, 2001), suggest: (1) that salt emergence was induced by localized fluvial entrenchment, rather than piercement of an overburden thinned by even erosional lowering; and (2) that the onset of salt extrusion occurred in late Quaternary times, rather than close to the Pliocene-Quaternary boundary. Passive diapirism began in the Cardener River valley and migrated laterally to the SW along the anticline hinge conditioned by the NE plunge of the fold. Salt flow can be driven by differential loading between the synclines and anticlines (fold-normal gradient) and between the valley margins and the valley floor (fold-parallel gradient).

The late Quaternary morpho-stratigraphic units documented along the margin of the salt diapir record an overall relief inversion trend. In an initial stage following the exposure of the salt, the rising salt extrusion was covered by rapid deposition of coarse-grained colluvium sourced from the surrounding high-relief country rock slopes. Differential uplift of the colluvial deposits by drape monoclinal folding resulted in the creation of upturned colluvial flaps and salt-edge elongated depressions. Lacustrine environments and marginal longitudinal valleys eventually developed in these laterally confined troughs. The late Pleistocene lake sediments and the late Holocene fluvial deposits with growth stratal geometries accumulated in these environments record long-term diapir activity (differential uplift and outward rotation). The diapir-flanking morpho-stratigraphic units can be ascribed to the two-end member types of halokinetic sequences described in sediments adjacent to steep passive diapirs deposited in the subsiding floor of sedimentary basins. The colluvial unit encroaching and onlaping the diapir corresponds to a wedge halokinetic sequence, whereas the nested lacustrine and fluvial deposits confined to the marginal depressions are comparable with hook halokinetic sequences. These types of sequences reflect the ratio between diapir rise rate and sedimentation rate, in agreement with the expectable rapid deposition of colluvial facies by mass wasting processes, and the slow aggradation of the fluvial and lake sediments, the latter estimated by radiocarbon dating at around 2–5 mm/yr. To our knowledge, this is the first work that documents late Quaternary halokinetic sequences in an erosional continental environment. Moreover, this study illustrates that the concepts and terms used to characterize halokinetic sequences in aggradational sedimentary basins can also be applied to erosional environments, where diapiric uplift can be recorded by both deformed sediments and landforms.

Halokinetic sequences typically develop in the sinking floor of sedimentary basins, where deposition adjacent to the rising diapir lack any outer lateral confinement. However, in the Cardona salt extrusion, located in the floor of a deep erosional depression, the steep country rock slopes act as a lateral confinement for deposition and as a backstop for the deformation induced by the uplift and outward rotation of the salt top. This explains the progressive upward and outward migration of the axis in the marginal depositional troughs and the significant degree of deformation of the deposits in the flaps, including shortening structures.

Long-term uplift rates ranging between 1.3 and 3.6 cm/yr have been estimated using the relative height and the age of radiocarbon dated deposits of raised strath terraces of the Cardener River and a tributary drainage. These rates are in agreement with published DiNSAR data. Uplift rate significantly decreases towards the edge of the salt extrusion may also show considerable along-strike variability within the salt wall. The relatively high salt rise values observed at the Cardona can be related to the youthful stage of the extrusion and the low viscosity of the Cardona Saline Formation, with a limited proportion of impurities and a considerable proportion of potash salts.

Author contributions

Conceptualization: FG; Data curation: All; Formal Analysis: All; Funding acquisition: FG; Investigation: All; Project administration: FG; Writing – original draft: FG; Writing – review & editing: All.

Declaration of competing interest

The authors declare that they have no known competing financial interests or personal relationships that could have appeared to influence the work reported in this paper.

Data availability

Data will be made available on request.

Acknowledgements

This work has been developed by DIAPERNO Project (PID2021-123189NB-I00) funded by the Spanish Government (Ministerio de Ciencia e Innovación). Authors are very grateful to the City Hall of Cardona for providing permission to dig the trench, Dr. Andreu Galera at the Cardona Archive for providing historical information, and Mr. Ferrán Climent (Director of Catalunya Central Geoparc) for logistic support. We also thank tow anonymous reviewers for their insightful comments.

References

Anadón, P., Cabrera, L., Colldeforns, B., Sáez, A., 1989. Los sistemas lacustres del Eoceno superior y Oligoceno del sector oriental de la Cuenca del Ebro. Acta Geol. Hisp. 24 (3–4), 205–230.

Autin, W.J., 2002. Landscape evolution of the Five Islands of south Louisiana: scientific policy and salt dome utilization and management. Geomorphology 47, 227–244.

Benito-Calvo, A., Moreno, D., Fujioka, T., López, G.I., Martín-González, F., Martínez-Fernández, A., Hernando-Alonso, I., Karampaglidis, T., Bermúdez de Castro, J.M., Gutiérrez, F., 2022. Towards the steady state? A long-term river incision deceleration pattern during Pleistocene entrenchment (Upper Ebro River, Northern Spain). Global Planet. Change 213, 103813.

Bruthans, J., Filippi, M., Zare, M., Churáčková, Z., Asadi, N., 2010. Evolution of salt diapir and karst morphology during the last glacial cycle: effects of sea-level oscillation, diapir and regional uplift, and erosion (Persian Gulf, Iran). Geomorphology 121 (3–4), 291–304.

Cardona, F., Viver, J., 2002. Sota la sal de Cardona. Espeleo Club de Gracia, Barcelona.

Colman, S.M., 1983. Influence of the Onion Creek salt diapir on the late Cenozoic history of Fisher Valley, southeastern Utah. Geology 11, 240–243.

Constable, S., Parker, R.L., Constable, C.G., 1987. Occam's inversion: a practical algorithm for generating smooth models from electromagnetic sounding data. Geophysics 52, 289–300.

Dahlin, T., Zhou, B., 2004. A numerical comparison of 2D resistivity imaging with 10 electrode arrays. Geophys. Prospect. 52, 379–398.

Davison, I., Bosence, D., Alsop, G.I., Al-Aawah, H., 1996. Deformation and sedimentation around active Miocene salt diapirs on the Tihama Plain, northwest Yemen. In: Alsop, G.I., Blundell, D.J., Davidson, I. (Eds.), Salt Tectonics, 100. Geological Society, London, Special Publication, pp. 23–39.

De Waele, J., Gutiérrez, F., 2022. Karst Hydrogeology, Geomorphology and Caves. Wiley, Chichester.

Del Santo, G., García-Sansegundo, J., Sarasa, L., Torrebadella, J., 2000. Estratigrafía y estructura del terciario en el sector oriental de la Cuenca del Ebro entre Solsona y Manresa (NE de España). Revista de la Sociedad Geológica Española 13 (2), 265–278.

Frumkin, A., 1996. Uplift rate relative to base-levels of a salt diapir (Dead Sea Basin, Israel) as indicated by cave levels. In: Alsop, G.I., Blundell, D.J., Davison, I. (Eds.), Salt Tectonics, 100. Geological Society, London, Special Publication, pp. 41–47.

García-Castellanos, D., Vergés, J., Gaspar-Escribano, J., Cloetingh, S., 2003. Interplay between tectonics, climate and fluvial transport during the Cenozoic evolution of the Ebro Basin (NE Iberia). J. Geophys. Res. 108, 2347. https://doi.org/10.1029/2002JB002073.B7.

Ge, H.X., Jackson, M.P.A., Vendeville, B.C., 1997. Kinematics and dynamics of salt tectonics driven by progradation. AAPG Bull. 81, 398–423.

Geometrics, 2009. SeisImager/2DTM Manual. Late access. https://www.geometrics.com/wp-content/uploads/2021/05/SeisImager2D_Documentation.zip. (Accessed 17 May 2023).

Giles, K.A., Rowan, M.G., 2012. Concepts in halokinetic-sequence deformation and stratigraphy. In: Alsop, G.I., Archer, S.G., Hartley, A.J., Grant, N.T., Hodgkinson, R. (Eds.), Salt Tectonics, Sediments and Prospectivity. Geological Society, London, Special Publication 361, pp. 7–31.

Gutiérrez, F., Lizaga, I., 2016. Sinkholes, collapse structures and large landslides in an active salt dome submerged by a reservoir: the unique case of the Ambal ridge in the Karun River, Zagros Mountains, Iran. Geomorphology 254, 88–103.

Gutiérrez, F., Linares, R., Roqué, C., Zarroca, M., Rosell, J., Galve, J.P., Carbonel, D., 2012. Investigating gravitational grabens related to lateral spreading and evaporite dissolution subsidence by means of detailed mapping, trenching, and electrical resistivity tomography (Spanish Pyrenees). Lithosphere 4, 331–353.

Gutiérrez, F., Sevil, J., Silva, P.G., et al., 2019. Geomorphic and stratigraphic evidence of Quaternary diapiric activity enhanced by fluvial incision. Navarrés salt wall and graben system, SE Spain. Geomorphology 342, 176–195.

Gutiérrez, F., Zarei, M., Hudec, M.R., Deirnik, H., 2023. Normal faulting and landsliding in morpho-structural domes related to buried salt stocks, Zagros Mountains, Iran. Insights into salt breakout. Mar. Petrol. Geol. 155, 106376.

Halbouty, M.T., 1979. Salt Domes, Gulf Region, United States & Mexico, Gulf Publishing, Houston, Texas.

Huntoon, P.W., 1982. The Meander anticline, Canyonlands, Utah: an unloading structure resulting from horizontal gliding on salt. Geol. Soc. Am. Bull. 93, 941–950.

Jackson, M.P.A., Hudec, M.R., 2017. Salt tectonics. Principles and Practice. Cambridge University Press, Cambridge.

Jochems, A.P., Pederson, J.L., 2015. Active salt deformation and rapid, transient incision along the Colorado River near Moab. Utah. In: Journal of Geophysical Research Earth Surface, 120, pp. 730–744.

Köthe, A., Hoffman, N., Krull, P., Zirngast, M., Zwirner, R., 2007. Geology of the overburden and adjoining rock of the Gorleben Salt Dome. Bundesanstalt für Geowisserschaften und Rohstofee.

Kravitz, K., Upton, P., Roy, S.G., 2017. Topographic controlled forcing of salt flow: three dimensional models of an active salt system, Canyonlands. Utah. J. Geophys. Res. Solid Earth 122, 710–733.

LaBrecque, D., Miletto, M., Daily, W., Ramirez, A., Owen, E., 1996. The effects of noise on Occam's inversion of resistivity tomography data. Geophysics 61, 538–548.

Lang, J., Hampel, A., Brandes, C., Winsemann, J., 2014. Response of salt structures to ice-sheet loading: implications for ice-marginal and subglacial processes. Quat. Sci. Rev. 101, 217–233.

Loke, M.H., 2011. Electrical resistivity surveys and data interpretation. In: Gupta, H. (Ed.), Solid Earth Geophysics Encyclopedia, second ed., Electrical & Electromagnetic. Springer-Verlag, Berlin, pp. 276–283.

Loke, M.H., Acworth, I., Dahlin, T., 2003. A comparison of smooth and blocky inversion method in 2D electrical tomography surveys. Explor. Geophys. 34, 182–187.

Lucha, P., Cardona, F., Gutiérrez, F., Guerrero, J., 2008. Natural and human-induced dissolution and subsidence processes in the salt outcrop of the Cardona Diapir (NE Spain). Environ. Geol. 53 (5), 1023–1035.

Luque, J.A., Julià, R., 2007. U/Th dating of Quaternary travertines at the middle river llogragat (NE iberian peninsula, northwestern mediterranean). Correlation with sea-level changes. Geol. Acta 5, 109–117.

Martin, R.G., Bouma, A.H., 1981. Active diapirism and slope steepening, northern Gulf of Mexico continental slope. Mar. Geotechnol. 5, 63–91.

Masana, E., Sans, M., 1996. Deformación neotectónica relacionada con anticlinales de núcleo salino (NE de la cuenca del Ebro, Barcelona). Geogaceta 20 (4), 846–849.

Moreno, D., Gutiérrez, F., del Val, M., Carbonel, D., Jiménez, F., Alonso, M.J., Martínez-Pillado, V., Guzmán, O., López, G.I., Martínez, D., 2021. A multi-method dating approach to reassess the geochronology of faulted Quaternary deposits in the central sector of the Iberian Chain (NE Spain). Quat. Geochronol. 65, 101185.

Nikolinakou, M.A., Flemings, P.B., Hudec, M.R., 2014. Modeling stress evolution around a rising salt diapir. Mar. Petrol. Geol. 51, 230–238.

Pardo, G., Arenas, C., González, A., Luzón, A., Muñoz, A., Pérez, A., Pérez-Riverés, F.J., Vázquez-Urbez, M., Villena, J., 2004. La Cuenca del Ebro. In: Vera, J.A. (Ed.), Geología de España. SGE-IGME, pp. 533–542.

Pérez-Rivarés, F.J., Arenas, C., Pardo, G., Garcés, M., 2018. Temporal aspects of genetic stratigraphic units in continental sedimentary basins: examples from the Ebro Basin, Spain. Earth Sci. Rev. 178, 136–153. https://doi.org/10.1016/j.earscirev.2018.01.019.

Pilcher, R.S., Kilsdonk, B., Trude, J., 2011. Primary basins and their boundaries in the deep-water northern Gulf of Mexico: origin, trap types, and petroleum system implications. AAPG Bull. 95 (2), 219–240.

Pirazzoli, P.A., Reyss, J.L., Fontugne, M., Haghipour, A., Hilgers, A., Kasper, H.U., Nazari, H., Preusser, F., Radtke, U., 2004. Quaternary coral-reef terraces from Kish and Qeshm Islands, Persian Gulf: new radiometric ages and tectonic implications. Quat. Int. 120 (1), 15–27.

Pueyo, J.J., 1975. Estudio petrológico y geoquímica de los yacimientos potásicos de Cardona, Suria, Sallent y Balsareny (Barcelona, España). PhD Thesis,. Universidad de Barcelona, unpublished.

Puigdefàbregas, C., Muñoz, J.A., Marzo, M., 1986. Thrust belt development in the Eastern Pyrenees and related depositional sequences in the southern foreland basin. In: Allen, P.A., Homewood, P. (Eds.), Foreland Basins. International Association of Sedimentologists Special Publication 8, pp. 229–246.

Reimer, P.J., Austin, W.E., Bard, E., Bayliss, A., Blackwell, P.G., Ramsey, C.B., Butzin, M., Cheng, H., Edwards, R.L., Friedrich, M., Grootes, P.M., Guilderson, T.P., Hajdas, I., Heaton, T.J., Hogg, A.G., Hughen, K.A., Kromer, B., Manning, S.W., Muscheler, R., Palmer, J.G., Pearson, Ch, van de Plicht, J., Reimer, R.W., Richards, D.A., Scott, E. M., Southon, J.R., Turney, Ch S.M., Wacker, L., Adolphi, F., Büntgen, U., Capano, M., Fahrni, S.M., Fogtmann-Schulz, A., Friedrich, R., Köhler, P., Kudsk, S., Miyake, F., Olsen, J., Reinig, F., Sakamoto, M., Sookdeo, A., Talamo, S., 2020. The IntCal20 Northern Hemisphere radiocarbon age calibration curve (0–55 cal kBP). Radiocarbon 62 (4), 725–757.

Reyss, J.L., Pirazzoli, P.A., Haghipour, A., Hatte, C., Fontugne, M., 1999. Quaternary marine terraces and tectonic uplift rates on the south coast of Iran. In: Stewart, I.S., Vita-Finzi, C. (Eds.), Coastal Tectonics. Geological Society, London, Special Publication 146, pp. 225–237.

Riba, O., Ramírez del Pozo, J., Maldonado, A., 1975. Mapa Geológico de España, 1: 50.000. Cardona (330). IGME, Madrid.

Riba, O., Reguant, S., Villena, J., 1983. Ensayo de síntesis estatigráfica y evolutiva de la cuenca terciaria del Ebro. In: Ríos, J.M. (Ed.), Geología de España, 2. Libro Jubilar IGME, pp. 131–159.

Rodríguez-Lloveras, X., Puig-Polo, C., Lantada, N., Gili, J.A., Marturià, J., 2020. Two decades of GPS/GNSS and DInSAR monitoring of Cardona salt mines (NE of Spain). Natural and mining-induced mechanisms and processes. Proceedings of the IAHS 382, pp. 167–172.

Rosell, L., Pueyo, J.J., 1997. Second marine evaporitic phase in the south pyrenean foredeep: the Priabonian potash basin (late Eocene: autochthonous–allochthobous zone). In: Busson, G., Schreiber, Ch (Eds.), Sedimentary Deposition in Rift and Foreland Basins in France and Spain. Columbia University Press, New York, pp. 358–387.

Rowan, M.G., Lawton, T.F., Giles, K.A., Ratliff, R.A., 2003. Near-salt deformation in La Popa basin, Mexico, and the northern Gulf of Mexico: a general model for passive diapirism. AAPG Bull. 87 (5), 733–756.

Rowan, M.G., Muñoz, J.A., Giles, K.A., Roca, E., Hearon IV, T.E., Fiduk, J.C., Ferrer, O., Fischer, M.P., 2020. Folding and fracturing of rocks adjacent to salt diapirs. J. Struct. Geol. 141, 104187.

Sáez, A., Riba, O., 1986. Depósitos aluviales y lacustres paleógenos del margen catalán de la Cuenca del Ebro. In: Anadón, P., y Cabrera, L. (Eds.), Guía de las excursiones del XI Congreso Español de Sedimentología, pp. 1–29. Barcelona.

Sans, M., 2003. From thrust tectonics to diapirism. The role of evaporites in the kinematic evolution of the eastern South Pyrenean front. Geol. Acta 1, 239–259.

Sans, M., Koyi, H.A., 2001. Modeling the role of erosion in diapir development in contractional settings. In: Koyi, H.A., Mancktelow, N.S. (Eds.), Tectonic Modelling: A Volume in Honor of Hans Ramberg. Geological Society of America, Memoir 193, pp. 111–122.

Sans, M., Verges, J., 1995. Fold development related to contractional salt tectonics: southeastern Pyrenean Thrust Front, Spain. In: Jackson, M.P.A., Roberts, D.G., Snelson, S. (Eds.), Salt Tectonics: a Global Perspective. AAPG Memoir 65, pp. 369–378.

Schultz-Ela, D.D., Walsh, P., 2002. Modeling of grabens extending above evaporites in Canyonlands National Park, Utah. J. Struct. Geol. 24, 247–275.

Sirocko, F., Szeder, T., Seelos, C., et al., 2002. Young tectonic and halokinetic movements in the Northern-German-Basin: its effect on formation of modern rivers and surface morphology. Neth. J. Geosci. 81, 431–441.

Stewart, S.A., 2006. Implications of passive salt diapir kinematics for reservoir segmentation by radial and concentric faults. Mar. Petrol. Geol. 23, 843–853.

Stuiver, M., Polach, H.A., 1977. Discussion reporting of 14C data. Radiocarbon 19, 355–363.

Talbot, C.J., 1998. Extrusions of Hormuz salt in Iran. In: Blundell, D.J., Scooott, A.C. (Eds.), The Past Is the Key to the Present. Geological Society, London, Special Publication 143, pp. 315–334.

Talbot, C.J., Jarvis, 1984. Age, budget and dynamics of active salt extrusion in Iran. J. Struct. Geol. 6, 521–533.

Talbot, C.J., Medvedev, S., Alavi, M., Shahrivar, H., Heidari, E., 2000. Salt extrusion rates at Kuh-e-Jahani, Iran: June 1994 to November 1997. In: Vendeville, B.C., Mart, Y., Vigneresse, J.L. (Eds.), Salt, Shale and Igneous Diapirs in and Around Europe. Geological Society, London, Special Publication 174, pp. 93–110.

Talbot, C.J., Pohjola, V., 2009. Subaerial salt extrusions in Iran as analogues of ice sheets, streams and glaciers. Earth Sci. Rev. 97, 155–183.

Urai, J.L., Scléder, Z., Spiers, C.J., Kukla, P.A., 2008. Flow and transport properties of salt rocks. In: Littke, R., Bayer, U., Gajewwwski, D., Nelsssskamp, S. (Eds.), Dynamics of Complex Intercontinental Basins: the Central European Basin System. Springer, Berlin, pp. 277–290.

Valle de Lersundi, J., 1999. Notas sobre el problema de Cardona (Unpublished report).

Van Keken, P.E., Spiers, C.J., van den Berg, A.P., Muyzert, E.J., 1993. The effective viscosity of rocksalt: implementation of steady-state creep laws in numerical models of salt diapirism. Tectonophysics 225, 457–476.

Vendeville, B.C., Jackson, M.P.A., 1992. The fall of diapirs during thin-skinned extension. Mar. Petrol. Geol. 9, 354–371.

Wagner, G., Mauthe, F., Mensik, H., 1971. Der salztock von Cardona in nordostpanien. Geol. Rundsch. 60, 970–996.

Warren, J.K., 2016. Evaporites: A Geological Compendium. Springer, Dordrecht.

Weinberger, R., Lyakhovsky, V., Baer, G., Begin, Z.B., 2006. Mechanical modelling and InSAR measurements of Mount Sedom uplift, Dead Sea basin: implications for effective viscosity of rock salt. Geochemistry, Geophysics, Geosystems 7, Q05014.